https://doi.org/10.1016/j.buildenv.2021.107740

The effects of lateral entrainment on pollutant dispersion inside a street canyon and the corresponding optimal urban design strategies

Zhengtong Li [a], Hao Zhang [a], Chih-Yung Wen [a], An-Shik Yang [b,*], Yu-Hsuan Juan [b]

[a] Department of Mechanical Engineering and Interdisciplinary Division of Aeronautical and Aviation Engineering, The Hong Kong Polytechnic University, Kowloon, Hong Kong

[b] Department of Energy and Refrigerating Air-Conditioning Engineering, National Taipei University of Technology, Taipei 106, Taiwan, ROC

* corresponding author

Abstract:

Intensive traffic emissions have caused many environmental problems and have a negative effect on public health. With the aim of mitigating these problems, it is essential to figure out how the flow structure affects the pollutant dispersion within the urban canopy. Most previous studies focus on the canopy vortex caused by top entrainment, but few previous studies are aware of the importance of lateral entrainment. By conducting computational fluid dynamic (CFD) simulations validated by wind tunnel data, we investigate the effects of lateral entrainment on pollutant dispersion inside a street canyon. Eight three-dimensional street canyons with various building heights and street lengths are considered. Besides, three optimal design strategies are proposed to improve the air quality by enhancing the lateral entrainment. The results of this analysis demonstrate that lateral entrainment could conditionally reduce the pollutant concentration of low-rise canyons. This reduction, which is affected by lateral entrainment, is confined in a range of approximately 2.5 times the street width from the street ends. In contrast, the lateral entrainment causes a more pronounced reduction in the pollutant concentrations of the high-rise canyons. Besides, all three strategies can considerably facilitate the lateral entrainment, leading to a significant reduction in the cross-section pollutant concentrations (by up to 76%) and therefore a significant reduction in the personal intake fraction P_IF of the residents (by up to 81%).

Keywords: Lateral entrainment; urban geometry; air quality; computational fluid dynamics; urban design strategies

1. Introduction

The ongoing global urbanization and accompanying intensive traffic emissions have given rise to many climatic and environmental problems [1], which significantly affect public health (e.g., respiratory and lung diseases) [2] and even cause considerable economic loss [3]. Evidently, air pollution has become one of the main concerns in the world, especially in metropolises. To alleviate the urban air pollution problem, one of the effective methods is to control the flow structure within urban areas [4,5]. This is because once these traffic emissions are discharged into the atmosphere, their dispersion is notably affected by the flow structure [6,7].

In most of the previous studies dealing with pollutant dispersion in canyons, the length of the street canyon was assumed to be infinite when the ambient wind was perpendicular to the street axis [8–11]. Consequently, the flow structure is mainly influenced by the top entrainment at the roof level of the infinite-long street canyon. At the roof level, a strong shear layer is developed due to the flow separation at the windward building edge [12]. From the building roof, the fresh air is entrained into the street canyon to form a clockwise recirculation with a horizontal (spanwise) axis (canyon vortex), which occupies the entire space of the street canyon [13]. Once the pollutants are emitted from street-level vehicles, most of the pollutants follow this canyon vortex, hence causing a higher concentration at the leeward side of the street canyons [14]. Then, the upward flow near the leeward surface will transfer to the external flow at the roof level. Since the length of the street canyon is assumed to be infinite, this clockwise recirculation in any cross-section of the street canyon is identical.

In effect, the length of the street canyon is finite [15,16]; thus, the lateral entrainment exists at the street ends. The two-dimensional (2D) simulations that consider only the top entrainment could not completely reflect the flow topology and pollutant dispersion processes in the entire street canyon [17]. At the same time, the influence of the lateral entrainment on the pollutant dispersion inside the street canyon has been confirmed in early studies. In a finite-long 3D street canyon, as seen in Fig. 1, the canyon vortex caused by the top entrainment usually appears nearby the center-plane of the street canyon [18]. However, at the ends of the street of a regular street canyon with $H/W = 1$, Hunter et al. [19] and Leitl and Meroney [20] found that there are double-eddy circulations (corner vortexs) with a vertical axis, entraining fresh air from the lateral shear layer (Fig. 1). Accordingly, the developed flow regime consists of a canyon vortex (caused by top entrainment) in the inner area and of two corner vortices (caused by lateral entrainment) at the street ends [21,22]. A superposition of the canyon vortex and the corner eddies results in a helical flow structure within the street canyon. Furthermore, Tsai et al. [23] reported that this helical flow structure causes along-street channeling flows toward the symmetry plane (the mid-plane in the spanwise direction) of the street canyons. Hence, the highest pollutant concentrations are on the symmetry plane. From this plane, the pollutant concentration decays symmetrically toward the street ends. Additionally, Gromke et al. [21] explained that a decrease in the pollutant concentration at the street ends is related to the enhanced ventilation by laterally entrained air. Accordingly, lateral entrainment can significantly affect the spanwise distribution of pollutants along a low-rise street canyon.

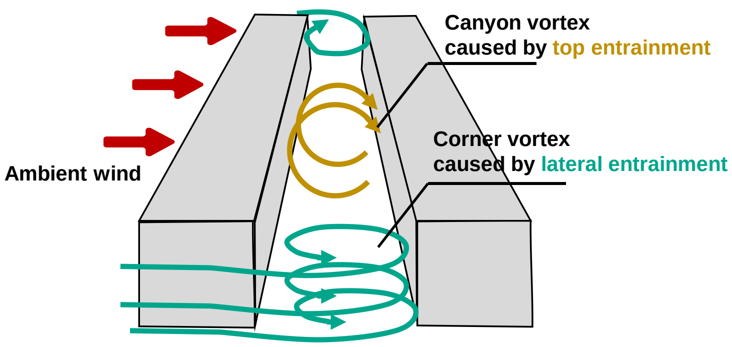

Fig. 1 Schematic illustration of the canyon vortex caused by the top entrainment and corner vortex caused by the lateral entrainment within a 3-D regular street canyon ($H/W = 1$) and subjected to perpendicular approaching wind.

Interestingly, the effectiveness of lateral entrainment on the flow in the street canyon has been found to vary with different configurations of street canyons. In the low-rise street canyon, Hunter et al. [19] found that the corner eddies caused by lateral entrainment were always maintained at the street ends, despite the increase in the street length. Similarly, Soulhac et al. [24] confirmed that these two corner eddies always penetrate toward the inner street-canyon area at approximately the order of the street width. Accordingly, the importance of the canyon vortex and the corner eddies changes with the building length (L) when the building height (H) and street width (W) are fixed. For example, Vardoulakis et al. [25] reported that in relatively low-rise short canyons ($L/W= 3$), the influence of the corner vortices might be strong enough to inhibit a stable vortex that is perpendicular to the street in the mid-plane of the spanwise direction. However, Mei et al. [26] showed that the influence of the corner eddies could be neglected when L/W is larger than 20 for a low-rise street canyon ($H/W= 1$). Furthermore, in a high-rise street canyon ($H/W= 2$), the threshold of L/W is 70 to neglect the corner eddies.

There is a large body of literature on the effects of top entrainment on the pollutant concentrations within the street canyon, while only a few studies address the effects of lateral entrainment. Most of these existing studies attempted to determine the situations when the lateral entrainment can be neglected in numerical simulations to simplify the 3D model to the 2D model [26]. Few of them could unravel the range and degree of the influence of lateral entrainment on the air quality when the geometry of the street canyons changes. Therefore, there is still a lack of sufficient understanding to fully utilize the positive effects of lateral entrainment on the air quality inside the canyons for practical urban planning.

On the other hand, the fact that enhanced ventilation by laterally entrained air causes lower pollutant concentrations at the street ends has been confirmed before. It can be inferred that enhancing the influence of lateral entrainment by certain optimal urban design strategies can effectively improve the dilution potential of air pollutants within the street canyon. However, as reviewed by previous literature, best urban design strategies focused on the enhancement of canyon vortexes by the top entrainment, such as a step-up street canyon [15,27], “lift-up” design (podium) [28], and arcade design [29,30]. Less attention has been paid to fully utilizing the positive effects of lateral entrainment on pollutant concentrations in terms of optimal urban design strategies.

In general, few previous studies are aware of the importance of lateral entrainment on the pollutant dispersion within street canyons, especially for the deep street canyon. Indeed, the distribution of pollutant inside canyons can be very sensitive to the lateral entrainment. Moreover, so far, the quantitative analysis of the influence of lateral entrainment is rare. Besides, previous studies have not determined how to effectively utilize the lateral entrainment to improve the air quality within the urban canopy. All these impose the need for investigating the effects of lateral entrainment on pollutant dispersion inside a street canyon and the corresponding optimal urban design strategies. Given this background, the objectives of this study are (1) to elucidate the mechanisms for how lateral entrainment affects the pollutant concentrations in the canyons with different geometries (different building heights and lengths), (2) to quantify the influence of lateral entrainment on the reduction of pollutant concentrations, for the canyons with different geometries (different building heights and lengths), compared with the infinite-long canyons alternative, and (3) to explore several optimal design strategies for improving the air quality within the street canyons by enhancing the lateral entrainment.

In section 2, a description of wind-tunnel experiments is presented. In section 3, the simulation details of the CFD setup are described, including the case study, model description, boundary conditions, numerical method, and grid sensitivity analysis. In section 4, we validate the present computational model with the turbulence modeling tested. In section 5, the mechanisms for how lateral entrainment affects the pollutant concentrations are discussed. Then, several optimal design strategies are proposed by utilizing lateral entrainment. Finally, the conclusions are given in section 6.

2. Description of wind tunnel experiments

Validation is obligatory to determine the accuracy and reliability of the results of CFD simulations [31]. The current computational model to reproduce the flow and concentration fields within street canyons was justified by a wind tunnel experiment conducted earlier at the Laboratory of Building and Environmental Aerodynamics, University of Karlsruhe [32,33]. The wind tunnel had a test section of 2 m long, 2 m wide, and 1 m high (Fig. 2(a)), in which a scaled model (1:150) of a three-dimensional isolated street canyon constructed by two parallel model-buildings with the dimension of $H \times W_b \times L$= 0.12 m × 0.12 m × 1.2 m (Fig. 2(b)) was tested. Meanwhile, the street width W is equal to the building width W_b. This isolated street canyon was simulated in a neutral atmospheric boundary layer (ABL) by using the vortex generators and a 5m long fetch covered with roughness elements (Fig. 2(a)). This combination produced a simulated boundary layer with a power-law exponent α of 0.30 and a friction velocity u^*_{ABL} of 0.52 m/s. The mean streamwise velocity profile of the approaching flow in the upstream can be approximated by using the following power-law form

$$U(z) = U_{ref} \times (z/H)^{0.3}, \tag{1}$$

where U_{ref} = 4.7 m/s is the reference velocity of the incoming flow at $z = H$ with a Reynolds number of approximately 37,600, based on the building height H and the reference velocity U_{ref}. Besides, Sulfur hexafluoride (SF6) was used as a tracer gas for simulating the release of traffic exhaust fumes and was emitted homogenously by four line-sources mounted at the bottom of the model. To account for the traffic exhaust fumes released on the street intersections, each line source exceeded the street canyon by approximately 10% on each side. For more information related to the wind-tunnel experiments, the reader is referred to [32,33]. Besides, it should be mentioned that the aforementioned wind tunnel experiment mainly offers concentration data within street canyons, including the canyon with trees and the canyon without trees. Herein, the free-tree case was chosen for the validation study.

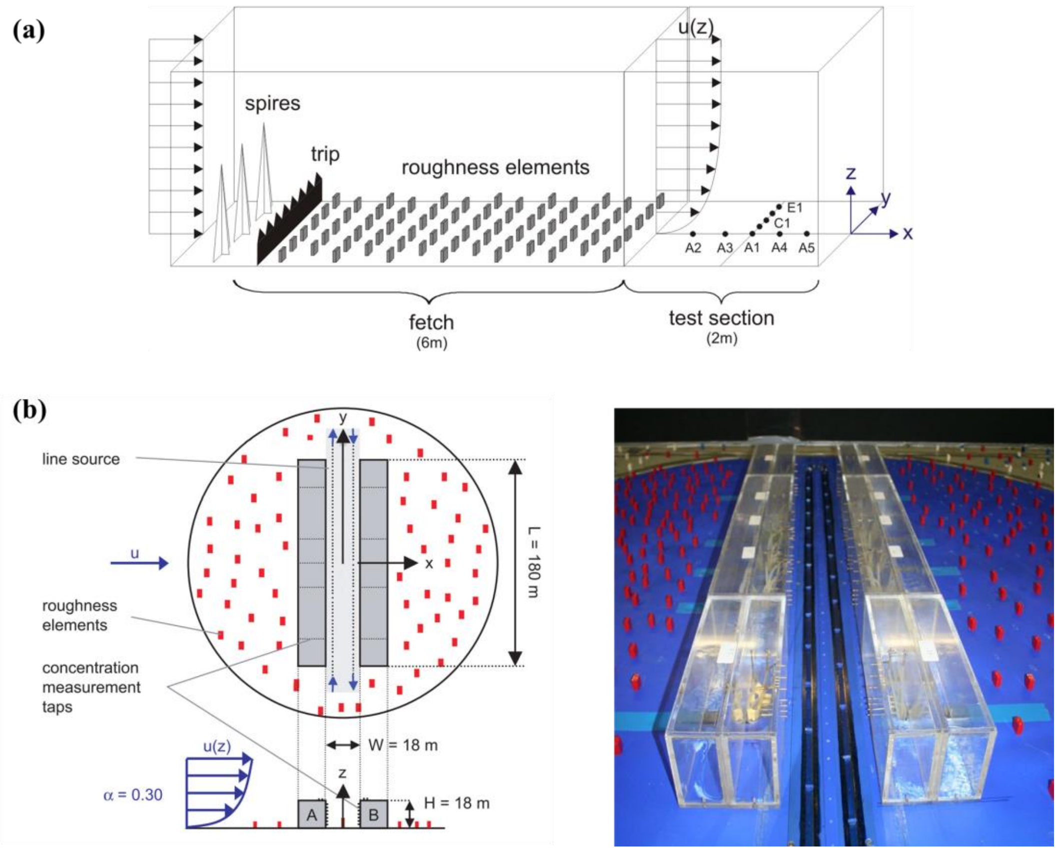

Fig. 2 Schematics of (a) test section of the wind tunnel, and (b) wind tunnel model of the urban street canyon (scale 1:150) [32,33]

3. Description of CFD simulations

3.1. Description of case studies, computational geometry and grid

The street canyon configurations used in the CFD simulations were constructed based on the scaled model (1:150) of an isolated street canyon adopted in the wind tunnel experiment mentioned above. Besides the configuration studied by the wind tunnel experiment, seven more configurations with various height and length aspect ratios, which are defined as H/W (= 1 and 3) and L/W (= 1, 5, 10, and ∞), were considered to investigate the effects of the lateral entrainment (Fig. 3(b)). These eight street canyons were first divided into two groups according to the aspect ratio of the building height to the street width (H/W), namely, the low-rise street canyons (H/W = 1) and high-rise street canyons (H/W = 3). Additionally, in each group, four aspect ratios of the building length to the street width (L/W) were considered, namely, the short street canyon (L/W = 1), the medium street canyon (L/W = 5), the long street canyon (L/W =

10), and the infinite-long street canyon ($L/W = \infty$), according to the classification of Oke et al. [34].

The size and discretization of the computational domain were referred from the practice guidelines by Tominaga et al. [35], thus the distances between the building and the inlet boundary, lateral boundaries, top boundary, and outflow boundary were 5 H, 5 H, 5 H, and 15 H, respectively, as shown in Fig. 3(a). The computational domain was discretized into approximately 2.8 million hexahedral cells for the low-rise medium street canyon (H/W = 1 and L/W = 5), as shown in Fig. 4. Considering the relatively large gradients of the velocity near the ground and building surfaces, the finest grids were deployed around these two types of walls. In this study, a grid-sensitivity analysis was performed based on two additional grids: a coarser grid and a finer grid for the low-rise medium street canyon case (Fig. A2). For the coarse, basic, and fine grids, the minimum sizes were set to be 0.006 m, 0.003 m, and 0.0015 m, respectively. The total cell numbers for the coarse, basic, and fine grids are 0.74 million, 2.83 million, and 9.66 million, respectively. Therefore, the ratios of the two consecutive cell numbers for the grid refinement meet the criterion of 3.4 in the mesh-independent study [35]. Then, the results of grid-sensitivity analysis discussed later indicate that the basic grid provides nearly grid-independent results, which can be further used for the remainder of this study.

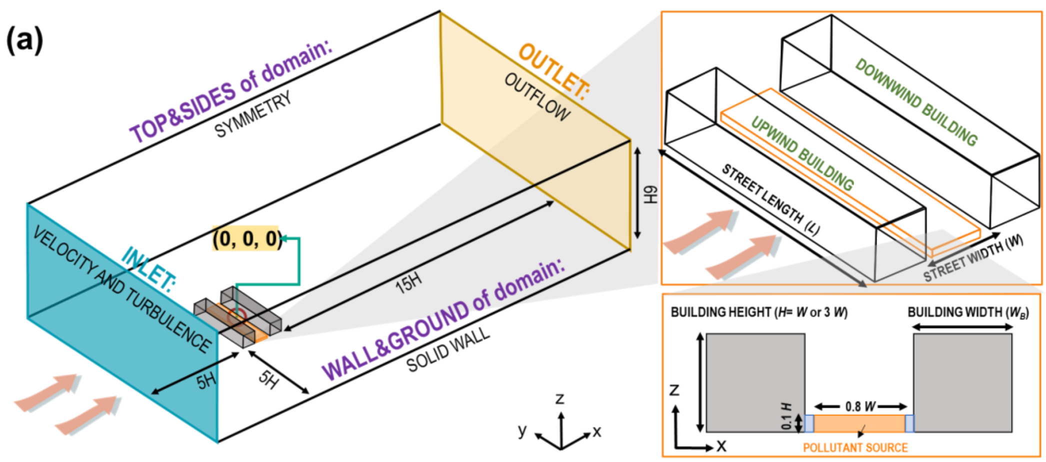

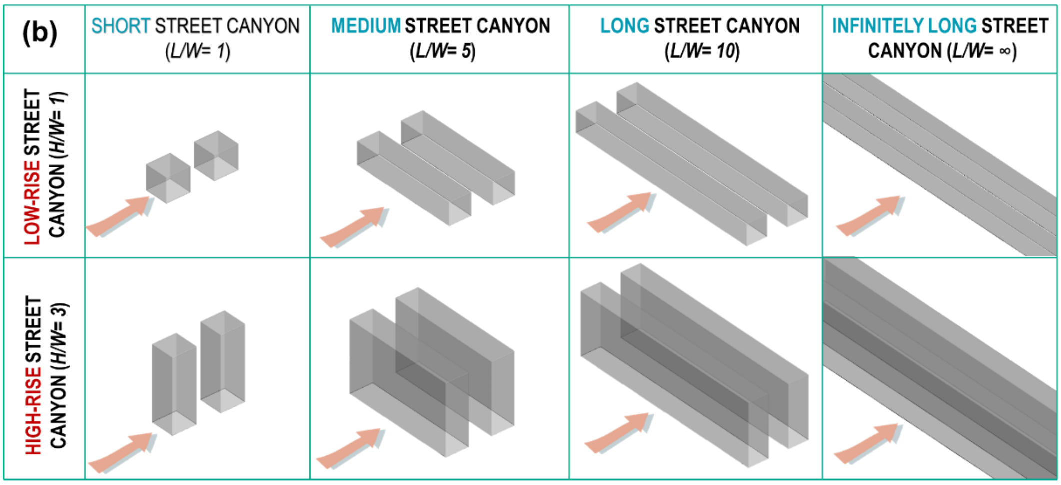

Fig. 3 (a) Computational geometry and boundary conditions; (b) 3D street canyon configuration with for high-rise and low-rise street canyons

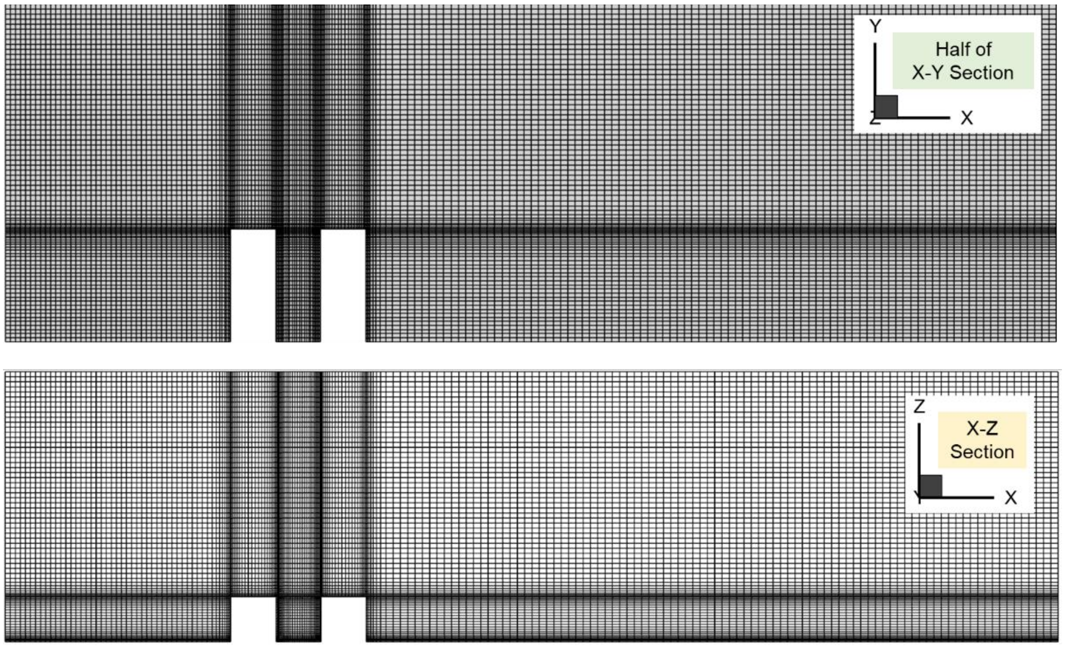

Fig. 4 Grid distributions of the geometric model:
$H/W = 1$ and $L/W = 5$ with the basic grid

3.2. Governing equation and turbulence model

The analyses were based on the steady-state 3D RANS conservation equations of mass and momentum for the incompressible turbulent flow. The governing equations are as follows:

Continuity equation:

$$\frac{\partial u_i}{\partial x_i} = 0, \tag{2}$$

Momentum equation:

$$\frac{\partial u_i u_j}{\partial x_j} = -\frac{1}{\rho}\left(\frac{\partial p}{\partial x_i}\right) + \frac{\partial \tau_{ij}}{\partial x_j}, \tag{3}$$

where the stress tensor τ_{ij} is defined as:

$$\tau_{ij} = \rho\left[\nu_t\left(\frac{\partial u_i}{\partial x_j} + \frac{\partial u_j}{\partial x_i}\right)\right] - \frac{2}{3}\rho k \delta_{ij}, \tag{4}$$

where the term u_i denotes the i-axis component of the air velocity; p and ρ represent the pressure and density; ν_t is the turbulent kinematic viscosity; δ_{ij} is the Kronecker delta; k is the turbulence kinetic energy.

The species transport equation was solved to probe the pollutant dispersion in an urban environment, as follows:

$$\frac{\partial u_i Y}{\partial x_i} - \frac{\partial}{\partial x_i}\left[\left(D + D_t\right)\frac{\partial Y}{\partial x_i}\right] = S_p, \tag{5}$$

where S_p is the pollutant source term (kg/(m^3·s)); D and D_t (= ν_t/Sc_t) denote the molecular and turbulent diffusion coefficients of the pollutant, respectively. Sc_t is the turbulent Schmidt number, which was set to 0.4 to account for the underestimation of the turbulent mass diffusion from the RANS models [36,37]. Y is the mass fraction of the pollutants. This dispersion of pollutants was simulated with the User Defined Scalar (UDS) option in ANSYS Fluent.

Moreover, the renormalization group (RNG) k-ε model [38] is chosen because of its generally good performance in predicting the flow separation by buildings and reversed flow [39], which is essential for the analysis of lateral entrainment in the present study. Also, the RNG k-ε model complements the disadvantage of a standard k-ε model, which overestimates turbulent kinetic energy near the edges of buildings where ambient flow impinges and separate [40]. Thus, the RNG k-ε model was used to solve this steady-state isothermal flow field. The conservation equations of the RNG k-ε turbulence model for the turbulence kinetic energy (k) and dissipation rate (ε) are as follows:

$$\frac{\partial u_j k}{\partial x_j} = \frac{\partial}{\partial x_j}\left(\frac{\nu_t}{\sigma_k}\frac{\partial k}{\partial x_j}\right) + P_k - \varepsilon \tag{6}$$

$$\frac{\partial u_j \varepsilon}{\partial x_j} = \frac{\partial}{\partial x_j}\left(\frac{\nu_t}{\sigma_\varepsilon}\frac{\partial \varepsilon}{\partial x_j}\right) + \frac{\varepsilon}{k}(C_{\varepsilon 1}^* P_k - C_{\varepsilon 2}\varepsilon) \tag{7}$$

In this equation, $P_k = \nu_t S^2$, $S = \sqrt{2S_{ij}S_{ij}}$, $S_{ij} = \frac{1}{2}\left(\frac{\partial u_i}{\partial x_j} + \frac{\partial u_j}{\partial x_i}\right)$, $\nu_t = C_\mu \frac{k^2}{\varepsilon}$, $\sigma_k = 1$, $C_{\varepsilon 1}^* = 1.42 - \frac{\eta(1-\eta/4.38)}{1+0.012\eta^3}$, $\eta = \frac{k}{\varepsilon}S$, $C_{\varepsilon 2} = 1.68$, and $\sigma_\varepsilon = 0.719$.

3.3. Boundary conditions

The measured inlet velocity profile from the wind tunnel experiments [32], which is given in Eq. (1), was used to characterize a neutral ABL. The turbulent kinetic energy k and turbulence dissipation rate ε profiles were calculated using Eqs. (8) and (9) [41]:

$$k = \frac{(u_{ABL}^*)^2}{\sqrt{C_\mu}}, \tag{8}$$

$$\varepsilon = \frac{(u_{ABL}^*)^3}{\kappa(z+z_0)}, \tag{9}$$

where u_{ABL}^* is the ABL friction velocity (= 0.52 m/s), κ is the von Karman's constant (= 0.42), z_0 is the aerodynamic roughness (= 0.0015 m), and C_μ is the model constant (= 0.085).

Besides, as seen in Fig. 3(a), the top and lateral boundaries of the domain were set as symmetry boundaries, namely setting normal velocity and normal gradients of all variables to zero. On the outlet of the domain, a zero diffusive flux was imposed for all flow variables in the direction normal to the outflow plane since the domain downstream was long enough to ensure a fully developed outlet flow. The standard wall functions by Launder and Spalding [42] with and without roughness modification by Cebeci and Bradshaw [43] were applied at the ground surface and building surface, respectively. To reduce horizontal inhomogeneity, the sand grain roughness height k_s is calculated by the roughness constant C_s (= 9.9) and the aerodynamic roughness z_0 (= 0.0015 m) in Eq. (10) [44].

$$k_s = \frac{9.793 z_0}{C_s}, \tag{10}$$

Besides, CO was used as the pollutant representative. To calculate the CO concentration, a uniform volume source (width $W_p = 0.8\ W$ and length L_p = street length L) of CO was specified near the ground with a depth of 0.1 H to represent the traffic lanes, as shown in Fig. 3(a). The constant emission rate per hour and unit street length (36.1 g/h/m, i.e., total mass release rate of $L_p \times 1.0 \times 10^{-5}$ kg/s) was adopted for each CO source with reference to Ng and Chau [45]. Considering the type and number of vehicles passing by a realistic street per hour in Mongkok, Hong Kong, Ng and Chau [45] summarized the pollutant release rate above.

3.4. Solver settings

The commercial software ANSYS/Fluent® CFD software (Release 15.0) [46] was used to simulate the airflow of ambient wind over this isolated street canyon. This study utilized the pressure-linked equations-consistent (SIMPLEC) numerical method for the pressure-velocity coupling. The second-order upwind scheme [47] was used to discretize both the convective terms and the diffusion terms. A double-precision solver was also selected for the CFD calculations. The convergence criterion of the normalized residual errors was set to 10^{-6} for the governing equations.

3.5 Grid sensitivity analysis

Three types of meshes were tested for the low-rise medium canyon under the same environmental conditions (U_{ref} = 4.7 m/s). Fig. 5 and 6 (a)-(c) depict a comparison of the results for the dimensionless streamwise mean velocity (u/U_{ref}) and dimensionless pollutant concentration (K) (defined in section 3.6) on the three grids along three vertical lines (x= -0.25H, 0, and 0.25H) in the vertical center plane at y/H = 0. Along these lines, the fine and the basic grid provide almost identical results, while some deviations are found between the coarse and the basic grid. Then, the grid convergence Index (GCI) proposed by Roache [48] (Eqs. (11) and (12)) is used to estimate the error of u/U_{ref} and K on the basic grid.

$$GCI_u = F_s \left| \frac{r^p (u_{basic} - u_{fine}) / U_{ref}}{1 - r^p} \right| \quad (11)$$

$$GCI_K = F_s \left| \frac{r^p (K_{basic} - K_{fine}) / K_{fine}}{1 - r^p} \right| \quad (12)$$

Where F_s is the safety factor taken as 1.25 when three or more grids are compared, r is the linear grid refinement ($=\sqrt{2}$), p is the former order of accuracy (=2), u and K are streamwise mean velocity and normalized concentration in one of the two grids (basic and fine), and U_{ref} is the reference wind speed of 4.7 m/s. The values of the GCI_u averaged along each vertical line are 0.04% for x/H = -0.25, 0.06% for x/H = 0, and 0.08% for x/H = 0.25 (Fig. 5 (d)-(f)). Similarly, the values of the GCI_K averaged along each vertical line are 1.80% for x/H = -0.25, 1.85% for x/H = 0, and 4.04% for x/H = 0.25 (Fig. 6 (d)-(f)). By analyzing the discrepancy in wind speed and pollutant concentration of the three grids as well as comparing GCI values of the Fine and Basic grids, it can be concluded that the basic grid provides nearly grid-independent results, which can be further used for the remainder of this study. Besides, the near-wall area was resolved by the standard wall functions directly on the condition that the $y+$ (a dimensionless wall distance to judge the applicability of wall functions [49], $y+ = u_T y / \nu$, where u_T is the friction velocity, y is the absolute distance from the wall, and ν is the kinematic viscosity) of the first near-wall mesh for building surfaces and ground was 167.7 on average, which was in the log-law layer $30 < y+ < 300$ [46,50].

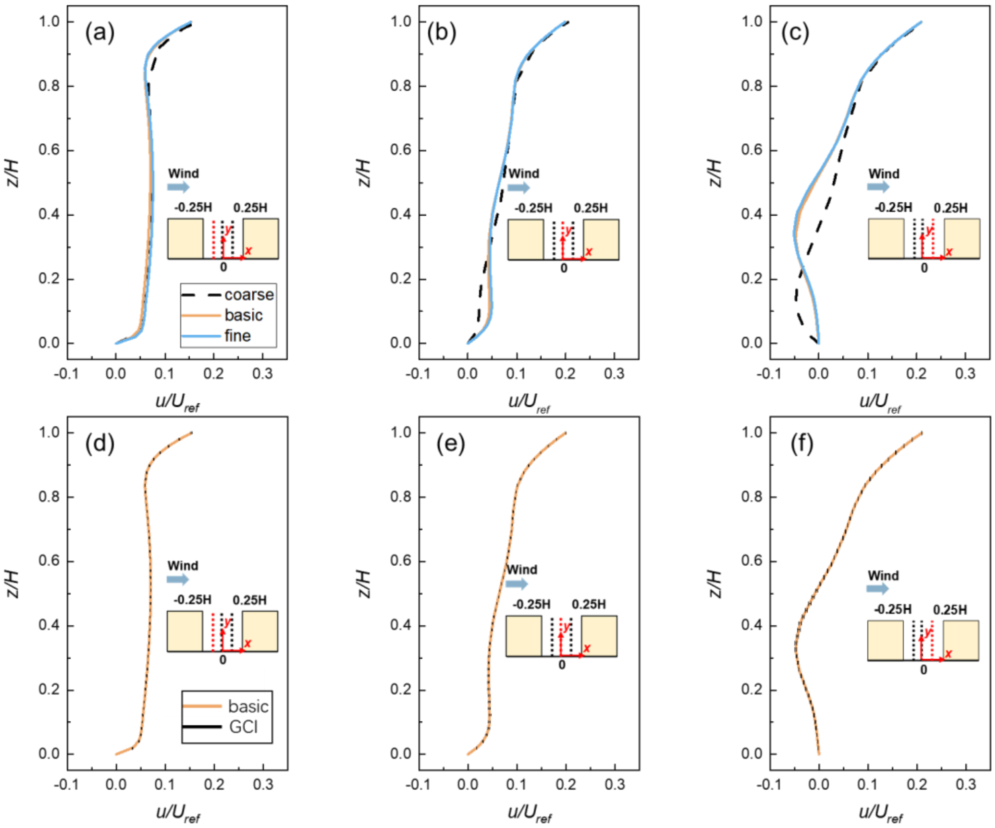

Fig. 5 (a-c) Comparison of dimensionless streamwise mean velocity (u/U_{ref}) along three vertical lines inside the street canyon in the vertical center plane in coarse, basic, and fine grids; (d-f) grid-convergence index (GCI) along the same three vertical lines.

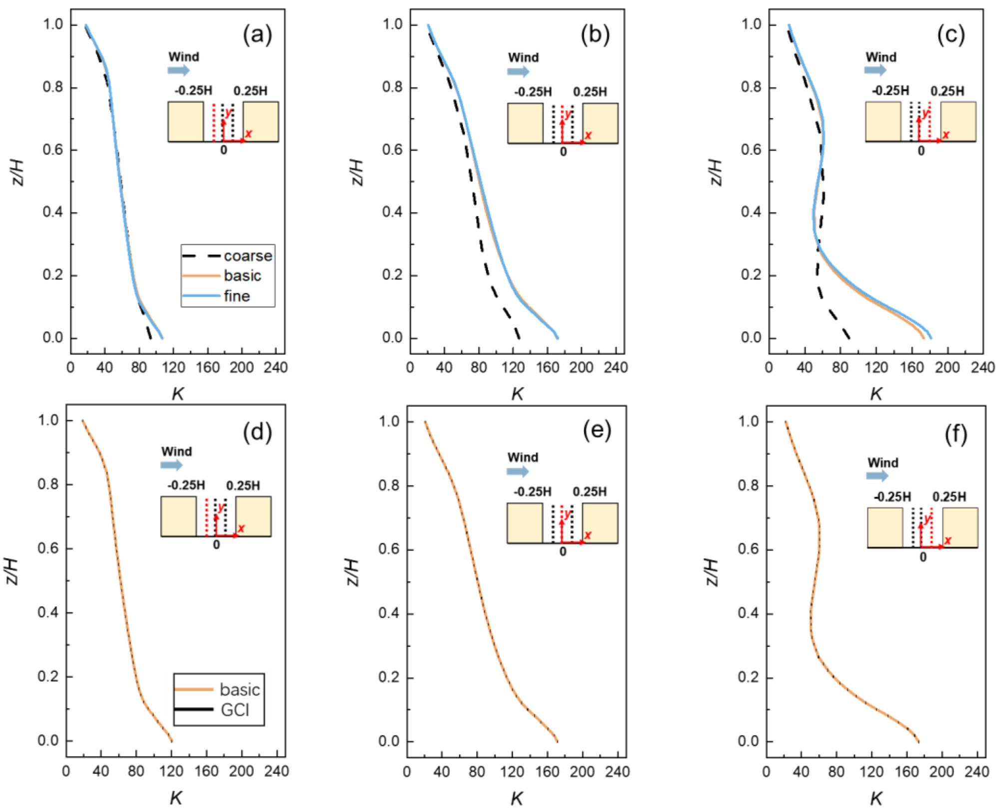

Fig. 6 (a-c) Comparison of dimensionless pollutant concentration K along three vertical lines inside the street canyon in the vertical center plane in coarse, basic, and fine grids; (d-f) grid-convergence index (GCI) along the same three vertical lines.

3.6 Air quality indices

3.6.1 Dimensionless pollutant concentration

In this study, the concentration of pollutants is mainly presented as dimensionless concentration K,

$$K = \frac{C U_{ref} H L}{S_p V_p} \tag{13}$$

Where C is the local pollutant concentration (kg/m^3); V_p is the volume of pollutant source (m^3).

3.6.2 Average dimensionless pollutant concentration

The lateral entrainment can significantly affect the spanwise distribution of pollutant concentrations along the street length. Therefore, the pedestrian-level and cross-section average dimensionless pollutant concentrations were introduced to better evaluate the effects of the lateral entrainment.

The average dimensionless pollutant concentration at the pedestrian-level (z = 1.5 m at full scale) along the street width was calculated by Eq. (14),

$$K_{ped} = \frac{\int_0^W K dx}{W} \tag{14}$$

The cross-section average dimensionless pollutant concentration along the street length was calculated in Eq. (15),

$$K_{cross} = \frac{\int_0^W \int_0^H K dx dz}{W \times H} \tag{15}$$

3.6.3 Personal intake fraction (*P_ IF*)

This study utilizes the personal intake fraction (*P_ IF*) as the air quality index, which stands for a fraction of the total traffic exhaust inhaled by each person on average, which was first introduced by Hang et al. [51] into CFD simulations to quantify the average personal exposure.

It is defined and calculated as follows:

$$P\_IF = \frac{\sum_i^N \sum_j^M P_i \times Br_{i,j} \times \Delta t_{i,j} \times Ce_j / m}{\sum_j^M P_i} \tag{16}$$

where N is the number of population groups (children, adults, elders, $N = 3$, $i = 1$ to 3), M is the number of different microenvironments (indoors at home, other indoor locations, near-vehicle locations, and other outdoor locations away from vehicles, M= 4, j= 1 to 4). Moreover, we assumed the following: the near-road buildings were residential, and only a microenvironment of j= 1 (indoor at home) was considered to assess the personal intake fraction for the local residents. $Br_{i,j}$ and $\Delta t_{i,j}$ are the average volumetric breathing rate (m^3/s) [51] (Table A1) and time spent (s) for individuals in the ith population group in the jth microenvironment [52] (Fig. A1(a)), respectively. P_i is the total number of people exposed in the ith population group, which can be further calculated by the demographic structure (herein, taking Shenzhen, China, as an example for this study [52], Fig. A1(b)). Ce_j is the pollutant concentration in the jth microenvironment (kg/m^3), which could be calculated from the average concentration at each floor (3 m). In this instance, m is the total pollutant emissions (kg).

4. Validation study

Before validation study and case study, a simulation was conducted with an empty computational domain to check the achievement of the horizontal homogeneity of ABL, since it is a prerequisite to a reliable prediction of pollutant dispersion within street canyons [53]. First, the inlet boundary conditions of the CFD simulation based on the experimental data (described in section 2) fit the inflow wind profile of the wind tunnel. Fig. A3 then shows a check of horizontal homogeneity for the present CFD simulation, which compared the dimensionless streamwise velocity and dimensionless turbulence kinetic energy of the inlet profile and incident profile (at the building position). The comparison indicates that the development of horizontal inhomogeneity is insignificant.

Besides, a solid model that included the street canyon ($H/W = 1$ and $L/W = 10$) was created by replicating the details of the geometrical shape from the wind tunnel experimental set-up of the tree-free case [32,33]. The computational domain was in line with the CFD set-up for the case study and pollutant sources were consistent with the wind tunnel setting. Moreover, the computational grid resolution resulted from a grid-sensitivity analysis, which yielded a fully structured hexahedral grid with 4.68 million cells. Then, a cross-comparison of the dimensionless vertical velocity at the $y/L = 0$ and the dimensionless pollutant concentration at the walls of the street canyon between the numerical and experimental results was presented in Fig. 7(a) and (b). The concentration value was calculated in the non-dimensional form as $C_+ = \frac{CU_{ref}H}{Q/l}$, where C is the measured concentration (g/m^3), and Q/l is the tracer gas source strength per unit length (g/m/s). Generally, the experimental and numerical distributions of the dimensionless vertical wind speed were consistent (Fig. 7(a)). Only on the windward side, the RNG k-ε turbulence model predicted slightly higher flow velocities. Then, two Sc_t ($Sc_t = 0.4$ and 0.7) were tested. As seen in Fig. 7 (b), the predicted dimensionless concentrations are similar to those obtained in the wind tunnel for both Sc_t. Nevertheless, the numerical results agree better with the wind tunnel data when $Sc_t = 0.4$. The RNG k-ε model with $Sc_t = 0.4$ was consequently adopted for our CFD simulations.

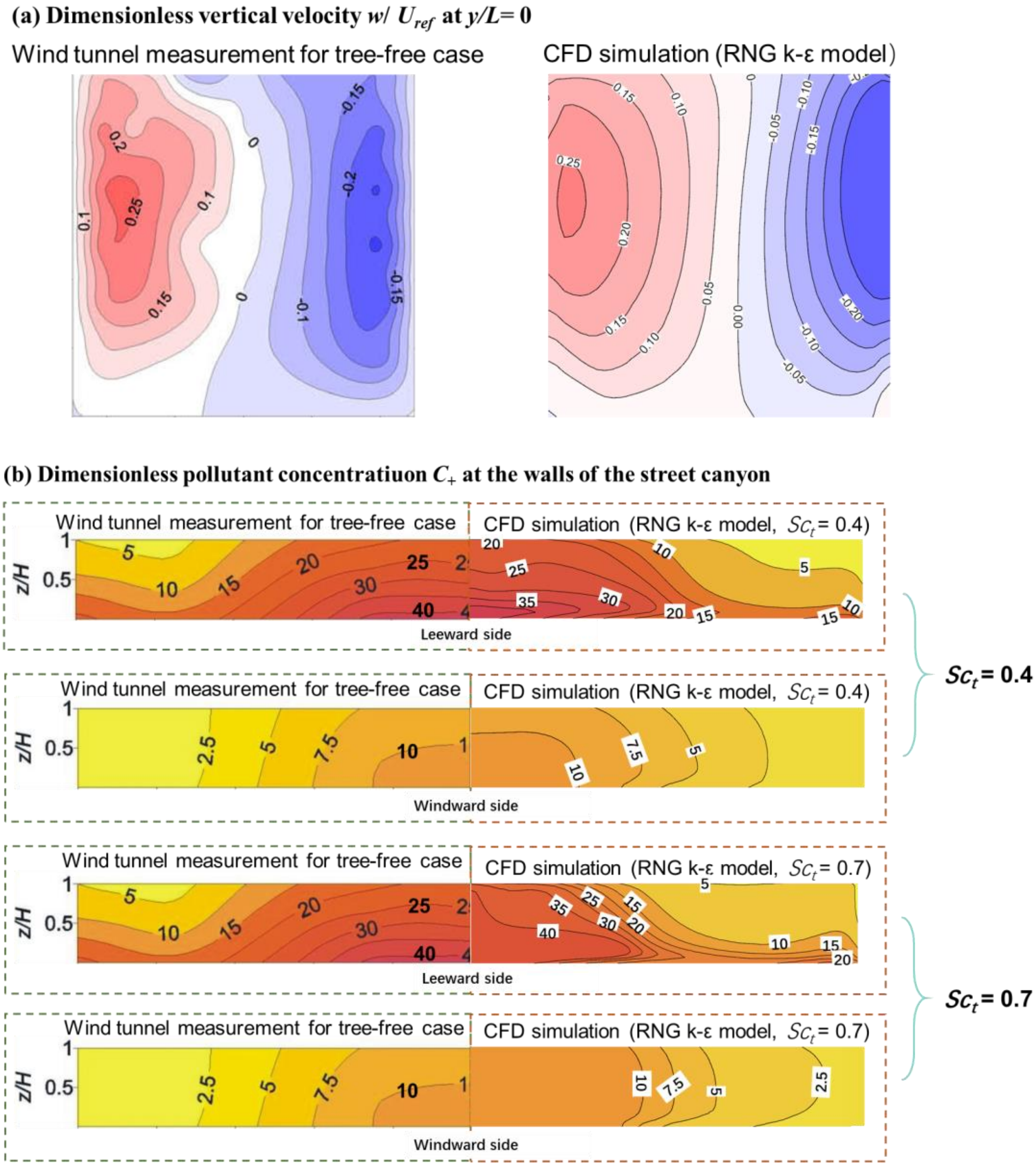

Fig. 7 Comparison results of (a) dimensionless vertical velocity at y/L = 0, and (b) dimensionless pollutant concentration at the walls of the street canyon.

5. Results and discussion

5.1 Effects of the lateral entrainment

5.1.1 Low-rise street canyon (H/W= 1)

The effects of the lateral entrainment on the low-rise street canyons (H/W= 1) are explored in this section. Figures 8 and 9 show the predicted dimensionless pollutant concentration K and dimensionless wind velocity (U/U_{ref}) contours for different street configurations at the pedestrian level and cross-section, respectively. To quantitatively estimate the effects, Fig. 10 compares the average pollutant concentrations at the pedestrian level and at various cross-sections.

In a low-rise infinite-long street canyon (H/W= 1 and L/W= ∞), the flow structure within the canyon was affected only by the top entrainment at the roof level. Thus, as seen in Fig. 9(a), the whole street canyon was occupied by the y-axis vortex. Evidently, this y-axis vortex in any cross-section of the infinite-long canyon would be identical, namely, a clockwise canyon vortex. Moreover, as evidenced in Fig. 8(a) and Fig. 9(a), there was relatively strong ventilation within this low-rise infinite-long street canyon since the top entrainment can readily penetrate into the ground level, thus leading to a lower dimensionless pollutant concentration at the pedestrian level (K< 66.5). In effect, in addition to the influence of the top entrainment, the airflow within the finite-long street canyon is also significantly affected by the lateral entrainment, which will be discussed later.

In a low-rise short street canyon (H/W= 1 and L/W= 1) in Fig. 9(b), the flow structure (3D streamlines) was still mostly dominated by the y-axis vortex caused by the top entrainment, which was similar to the infinite-long street canyon in Fig. 9(a). In contrast, the pedestrian level was occupied by the outward airflows (the along-street channeling flows toward the street ends) (Fig. 8(b)). The possible reason was that the lateral entrainment caused a pair of corner vortices at the pedestrian level of the street ends. Following these corner vortices, the wind flowed outward along the leeward side of the upwind building. As a result of this marked outward airflow, the maximum pedestrian level concentration was notably reduced by almost 65% (Fig. 8(b)), and the average pedestrian level concentration decreased by 65-73% along the street length, as well (Fig. 10(a)), compared with the infinite-long street canyon. At the same time, as seen in Fig. 9(b), the wind velocity was enhanced at all of the cross-sections. The upward transportation of the pollutants was also improved, which led to a significant reduction in the concentration at all of the cross-sections. Figure 10(b) further confirmed that the average cross-section concentration remarkably decreased by almost

73-77% along the street length due to the lateral entrainment.

In a low-rise medium street canyon (*H/W*= 1 and *L/W*= 5), there existed two evident corner vortices at the street ends (Fig. 8(c)), although the 3D streamlines were still dominated by the *y*-axis vortex (Fig. 9(c)). On the other hand, except for the region covered by the corner vortices, as shown in Fig. 8(c), the whole pedestrian level was mainly occupied by the inward flows (along-street channeling flows toward the symmetry plane). In effect, these inward channeling flows can be attributed to the superposition of the canyon vortex (caused by the top entrainment) and the corner vortex (caused by the lateral entrainment). These inward channeling flows enhanced the pedestrian level dimensionless wind velocity (up to nearly 0.1) and then transported the pollutants toward the symmetry plane (Fig. 8(c)). Consequently, as seen in Fig. 10 (a), in almost 65% of the region of the street canyon, the concentration significantly decreased, especially at the street ends (by up to 70%). However, the concentration increased in the remaining 35% region of the street canyon near the symmetry plane (by up to 86%). This trend occurred because the accumulating pollutants in the canyon-center region caused by the inward channeling flow could not be dispersed upward effectively along with the canyon vortex, which was further confirmed in Fig. 9(c). Clearly, the wind velocity in most inner section of this medium street canyon was lower than that in the infinite-long case, thus leading to a significant increase in the pollutant concentration, especially near the ground. Therefore, Fig. 10 (b) reported that the cross-section average concentration declined by up to 78% from *y/L*= 0.17 to 0.5, while it increased by up to nearly 117% from *y/L*= 0 to 0.17.

In a low-rise long street canyon (*H/W*= 1 and *L/W*= 10), similar to the medium street canyon, the corner vortices and the inward channeling flow were clearly observed in Fig. 8(d). In contrast, the inward channeling flow only penetrated approximately 2.5 times the street width from the street ends (Fig. 8(d)). Furthermore, in the inner region of the canyon (from *y/L*= 0.3 to 0), the airflow was almost dominated by the *y*-axis vortex (canyon vortex), which was similar to the infinite-long street canyon (from the windward side of the downwind building to the leeward side of the upwind building).

Accordingly, the pedestrian level dimensionless velocity was significantly enhanced by up to 0.17 from only y/L= 0.5 to 0.25, but it decreased by approximately 0.1 in the inner region of the canyons (Fig. 8(d)), compared with the infinite-long street canyon. As a result, the average pedestrian level concentration decreased by up to almost 78% in the outer region of the canyon, but it significantly increased in the inner region of the canyon, especially from y/L= 0.28 to 0 (even by almost 50%) (Fig. 10(a)). On the other hand, as seen in Fig. 9(d), a lower wind velocity was found in the inner three sections, which further deterred the upward dispersion of the pollutants. Obviously, as shown in Fig. 9(d) and Fig. 10(b), the cross-section average concentration increased by up to 34%, from y/L= 0.27 to 0.

Overall, it is concluded that in the low-rise street canyon (H/W= 1), the lateral entrainment can partially improve the air quality, depending on the street length. This finding occurred because the positive effects of lateral entrainment on the pollutant concentration inside the street canyon were confined in a range of approximately 2.5 times the street width from the street ends (Fig. 8(d)). Therefore, the lateral entrainment was of great importance in reducing the pollutant concentration of the short and medium street canyon. However, the air quality of the low-rise long canyon could only be improved in the outer half of the street length by the lateral entrainment.

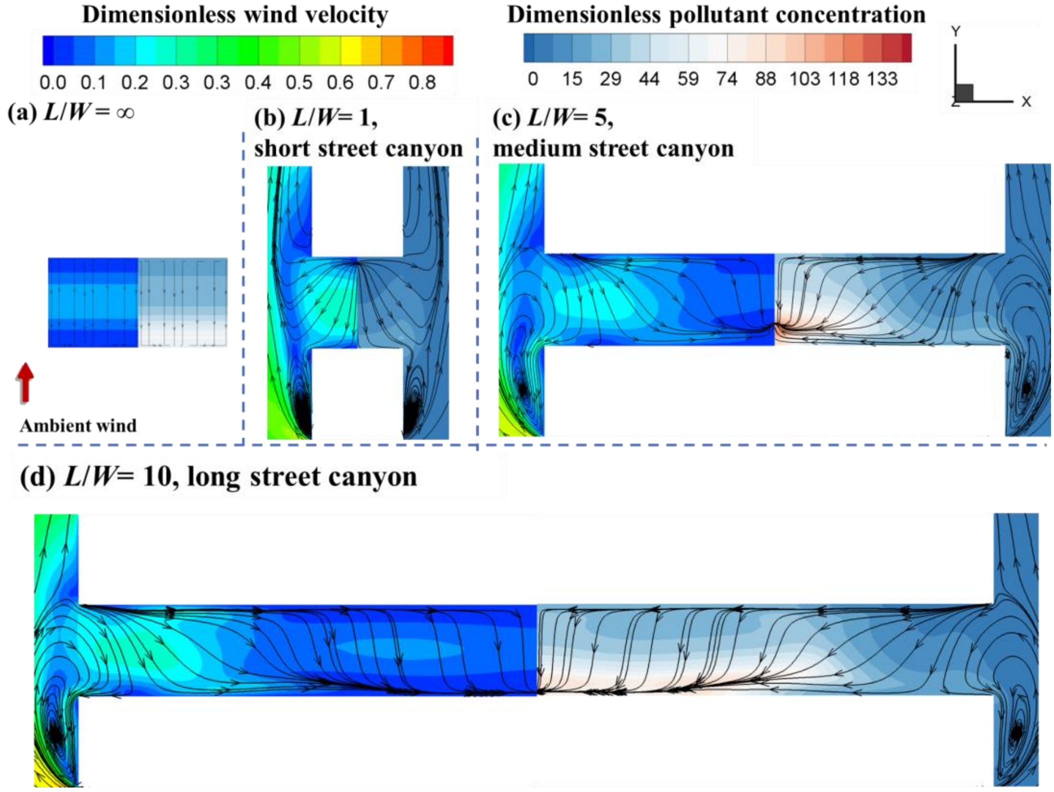

Fig. 8 Predicted pedestrian level pollutant concentration contours, and pedestrian level wind velocity contours for the low-rise street canyons (H/W= 1) with various street lengths: (a) L/W= ∞, infinite-long street canyon, (b) L/W= 1, short street canyon, (c) L/W= 5, medium street canyon, and (d) L/W= 10, long street canyon.

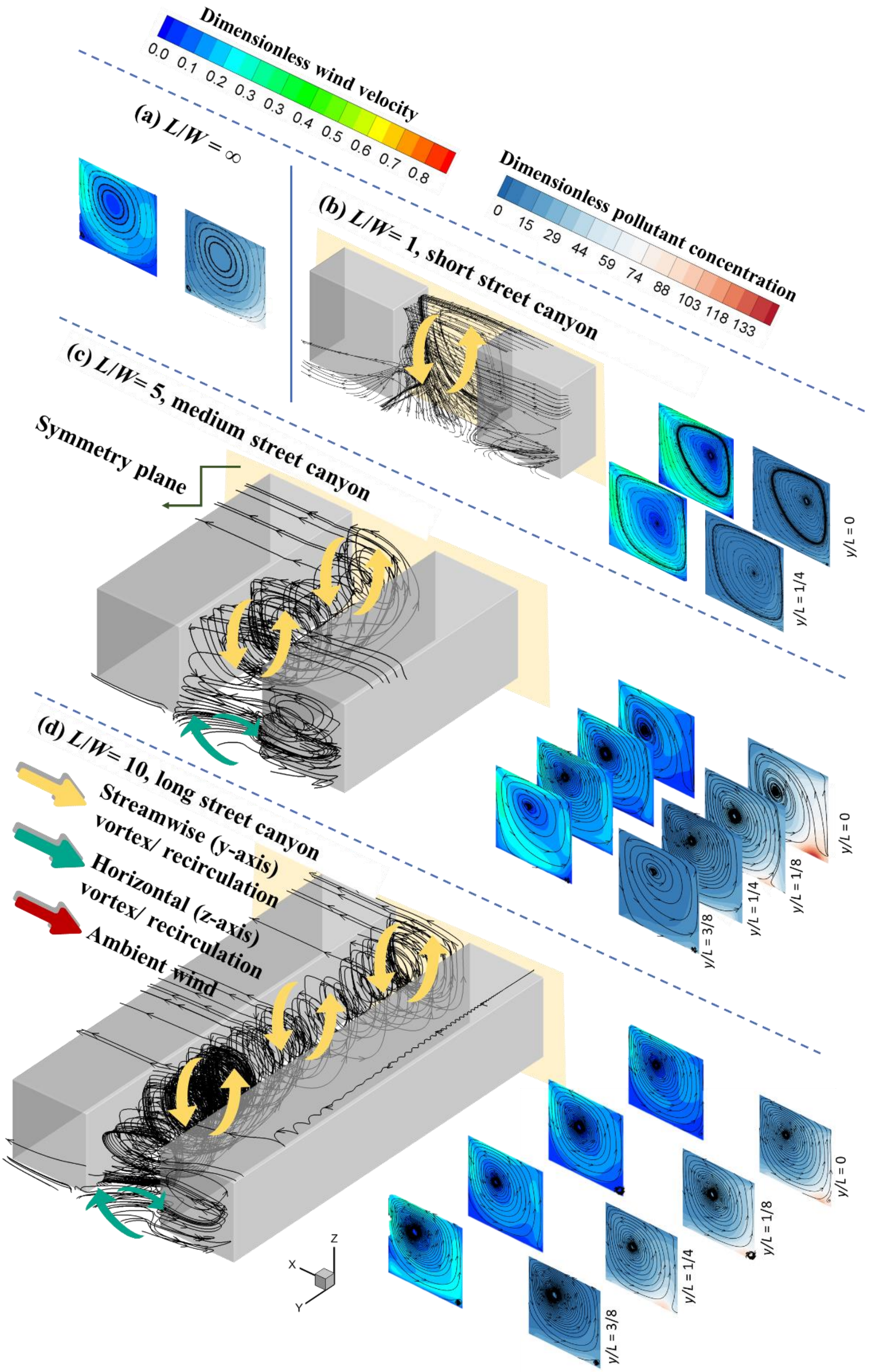

Fig. 9 Predicted 3D streamlines, *x-z* cross-section pollutant concentration and wind velocity contours for the low-rise street canyons (*H/W*= 1) with various street

lengths: (a) $L/W= \infty$, infinite-long street canyon, (b) $L/W= 1$, short street canyon, (c) $L/W= 5$, medium street canyon, and (d) $L/W= 10$, long street canyon.

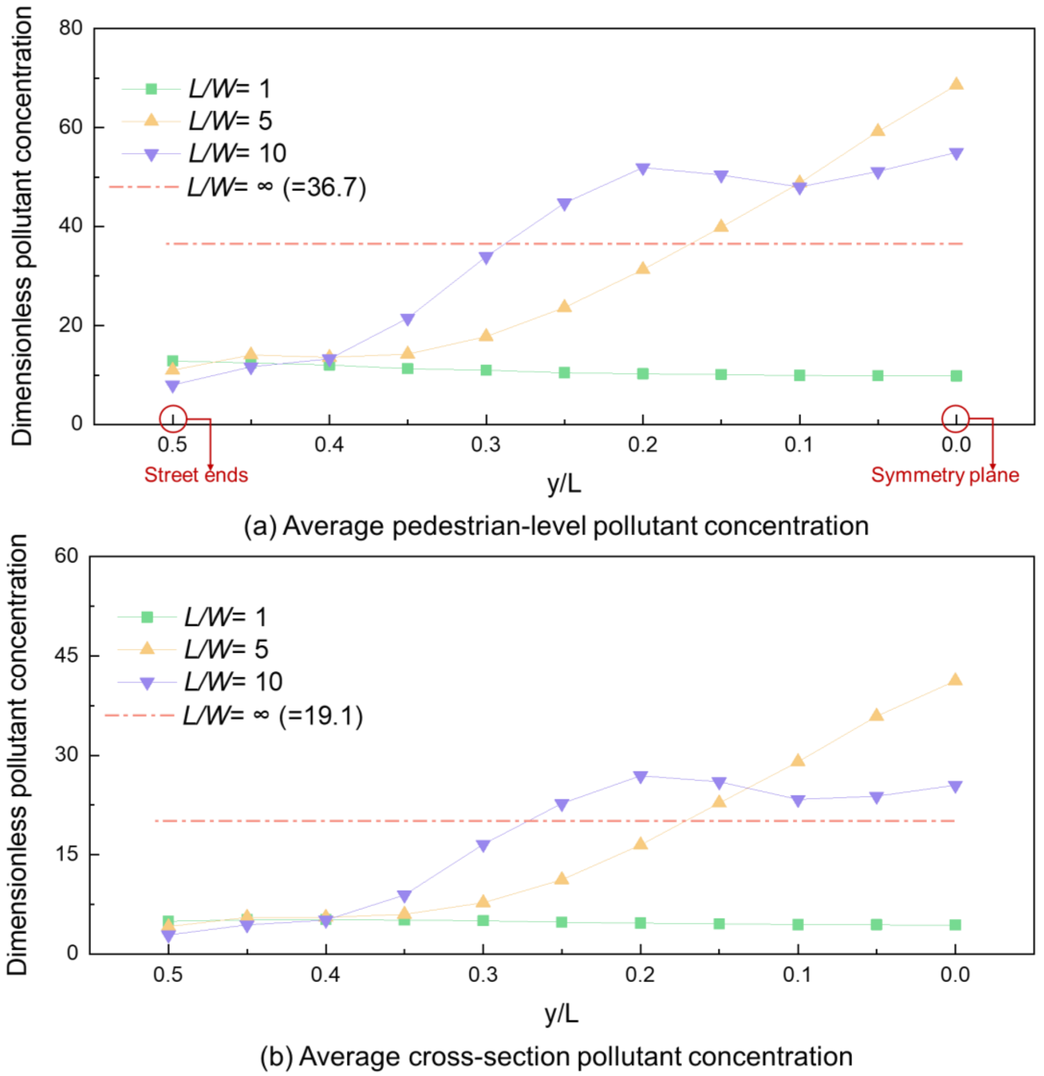

Fig. 10 Average pollutant concentration along half of the street length for the low-rise street canyon ($H/W= 1$) with various street lengths: (a) average pedestrian level pollutant concentration, and (b) average cross-section pollutant concentration

5.1.2 High-rise street canyon ($H/W= 3$)

To discuss the influence of the lateral entrainment on high-rise street canyons, the numerical results on the dimensionless wind velocity and pollutant concentration are presented at the pedestrian level in Fig. 11 and for various *x-z* cross-sections in Fig. 12; at the same time, the average pollutant concentrations for different street lengths are compared in Fig. 13.

Within a high-rise infinite-long street canyon ($H/W= 3$ and $L/W= \infty$), as seen in Fig.

12(a), the top entrainment from the roof level induced two vertically aligned vortices (y-axis vortex). Consequently, Fig. 12(a) showed that it was pretty difficult for the top entrainment to penetrate downward into the pedestrian level where the traffic emission sources were located. The airflow within the lower two y-axis canyon vortices was too slow (dimensionless wind velocity< 0.02) to generate any upward pollutant dispersion (Fig. 12(a)). In other words, the upward advective transport of the airflow had little contribution to the dispersion process of the pollutants (transporting the pollutant from the lower recirculation to the upper recirculation and eventually toward the roof level). Accordingly, it was evident that there existed a substantial pollutant accumulation in the lower part of the high-rise canyon (Fig. 11(a) and Fig. 12(a)). The highest pollutant concentration in the lower space was almost one order higher than that at the roof level. Interestingly, these results were inconsistent with the field measurements by Zhang et al. [54] in a similar deep street canyon ($H/W \approx 2.7$ and $L/W \approx 10$). As reported by Zhang et al. [54], the highest low-level concentration was only two times higher than the roof-level concentration. Thus, it could be deduced that the airflow was possibly sensitive to the lateral entrainment within a finite-long high-rise street canyon, which might extensively promote the pollutant dispersion in the lower space.

In the high-rise short street canyon ($H/W= 3$ and $L/W= 1$) in Fig. 12(b), the top entrainment produced two separated y-axis vortices compared with the infinite-long counterpart. Interestingly, at the pedestrian level, there were noticeable divergent and outward airflows caused by lateral entrainment (Fig. 11(b)). Although the pedestrian level wind speed was still relatively low, the pollutants could be effectively transported outward along with these divergent flows. In consequence, as seen in Fig. 13(a), the average pedestrian level concentration was reduced by almost up to 98% along the street length, compared with the infinite-long counterpart. In other words, the lateral entrainment could affect the pollutant dispersion of whole street canyon. Furthermore, the wind velocity and flow patterns of the various x-z cross-sections showed that the canyon was almost occupied by the strong downward airflows (Fig. 12(b)). At the same time, the dimensionless wind velocity at the cross-section was enhanced by up to 0.5

(Fig. 12(b)). Accordingly, the pollutants only slightly accumulated near the ground level (Fig. 12(b)). Figure 13(b) reported that the average concentration of the x-z section decreased by up to 99% along the street length.

In a high-rise medium street canyon (H/W= 3 and L/W= 5), similar to the short canyon, the top entrainment still caused a y-axis vortex near the roof level (Fig. 12(c)). In contrast, the lateral entrainment produced two symmetric spanwise recirculation in the lower space. As evidenced in Fig. 11(c), the outer regions ($0.35 < y/L < 0.5$) were dominated by the outward airflows at the pedestrian level. Instead, in the inner regions ($0 < y/L < 0.35$), there existed the inward channeling airflows. Therefore, a higher pollutant concentration was found near the symmetry plane. Compared with the infinite-long case (Fig. 11(a)), the medium street still had a markedly smaller magnitude of the concentration with the same level of wind velocity (Fig. 11(c)). As also shown in Fig. 13(a), the average pedestrian level concentration was reduced by 81 - 98%. A possible explanation lies in the stronger advective transport of pollutants provided by the x-axis recirculation, which could be substantiated in the flow patterns and wind velocity contours of various x-z cross-sections (Fig. 12(c)). In the inner two sections, there was an upward airflow with a higher wind velocity; thus, the pollutants within the street center region could be more substantially transported out across the roof level. Compared to the results of the infinite-long case, the pollutant concentration decreased remarkably due to the lateral entrainment for all of the x-z cross-sections (Fig. 12(c)), and the average concentration along the street length was reduced by 75 - 98% (Fig. 13(b)).

As shown in Fig. 12(d), in a high-rise long street canyon (H/W= 3 and L/W= 10), the flow patterns were slightly different from those in the short and medium street canyons. Nevertheless, the y-axis and x-axis vortex dominated the pollutant transport in the upper and lower spaces, respectively. Furthermore, the x-axis vortex was elongated. This x-axis vortex caused clear inward channeling flows at the pedestrian level, transporting most of the pollutants toward the symmetry plane and leading to a more significant pollutant accumulation in the street center region, compared with the shorter canyons (short and medium street canyons). As shown in Fig. 13(a), although the maximum pedestrian level concentration of the long street canyon was up to 10 times higher than its shorter counterparts, this maximum value was still much lower than the infinite-long street result. On the other hand, as seen in Fig. 12(d), although the wind velocity in the lower part of most inner section began to be stagnant, the x-axis vortex could still reinforce the upward advective transportation of the pollutants. Therefore, the maximum average cross-section concentration was almost three times lower than the infinite-long counterpart (Fig. 13(b)). Besides, this high-rise long street canyon (H/W= 3 and L/W= 10) shares a similar configuration with the study of Zhang et al. [54]. The measurement position by Zhang et al. [54] is nearly 0.3L away from the street ends. The low-level concentration was two times higher than the roof-level concentration. In the present study (Fig. 12 (c)), the low-level concentration of the second section (y/L= 1/4) from the street ends was nearly 3-4 times higher than the roof-level concentration. The difference between this CFD simulation and field measurement is reasonable, and they are in the same order. Notably, the realistic traffic-induced turbulence [55], solar radiation [56], and building separation [45] (were not considered in the present study) can also improve the pollutant dispersion, especially for the low-space of street canyon.

In general, in the high-rise street canyons, the lateral entrainment can reduce the pollutant concentration more significantly, compared with the low-rise street canyons. The reason is that the lateral entrainment can entirely affect the x-axis vortex/ recirculation in the lower part of the canyon; hence, it can increase the vertical advective transportation of the pollutants in the canyon's center region. With an increase in the street length, the flow patterns remained unchanged, with the dominated y-axis vortex in the most upper space and x-axis vortex/recirculation in the lower space, respectively, but the influence of lateral entrainment on the pollutant concentration became weaker. Despite this effect, the concentrations for the short, medium, and long canyons were still far lower than that of the infinite canyon. In consequence, these phenomena demonstrated that the lateral entrainment significantly contributed to the pollutant dispersion for these high-rise street canyons. Moreover, compared with the low-rise canyon, the high-rise canyon has a significantly higher concentration, especially for the longer street length. Taking the infinite-long canyon as examples, the pedestrian level average pollutant concentration of high-rise canyon (=769.3) is about 20 times that of the low-rise canyon (=36.7), which is in line with the study of Assimakopoulos et al. [11]. Accordingly, it indicates that weaker top entrainment in high-rise canyon greatly limits the dilution of pollutants.

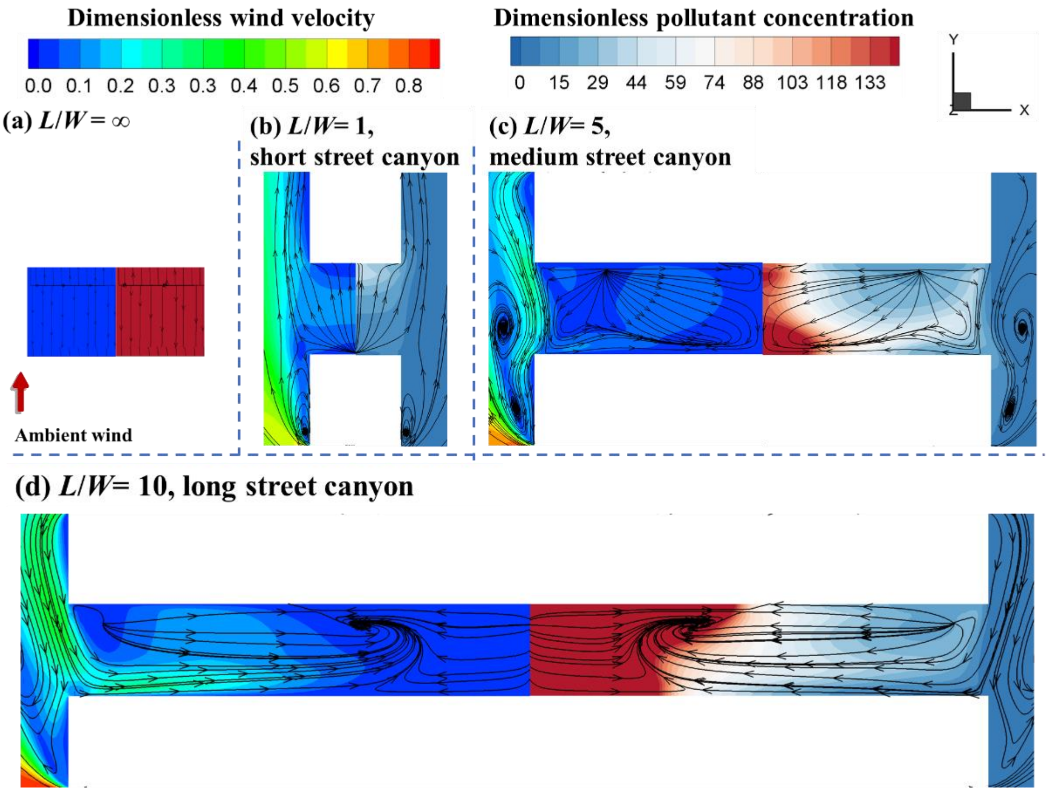

Fig. 11 Predicted 3D streamlines, pedestrian level pollutant concentration contours, and pedestrian level wind velocity contours for the high-rise street canyons (*H*/*W*= 3) with various street lengths: (a) *L*/*W*= ∞, infinite-long street canyon, (b) *L*/*W*= 1, short street canyon, (c) *L*/*W*= 5, medium street canyon, and (d) *L*/*W*= 10, long street canyon.

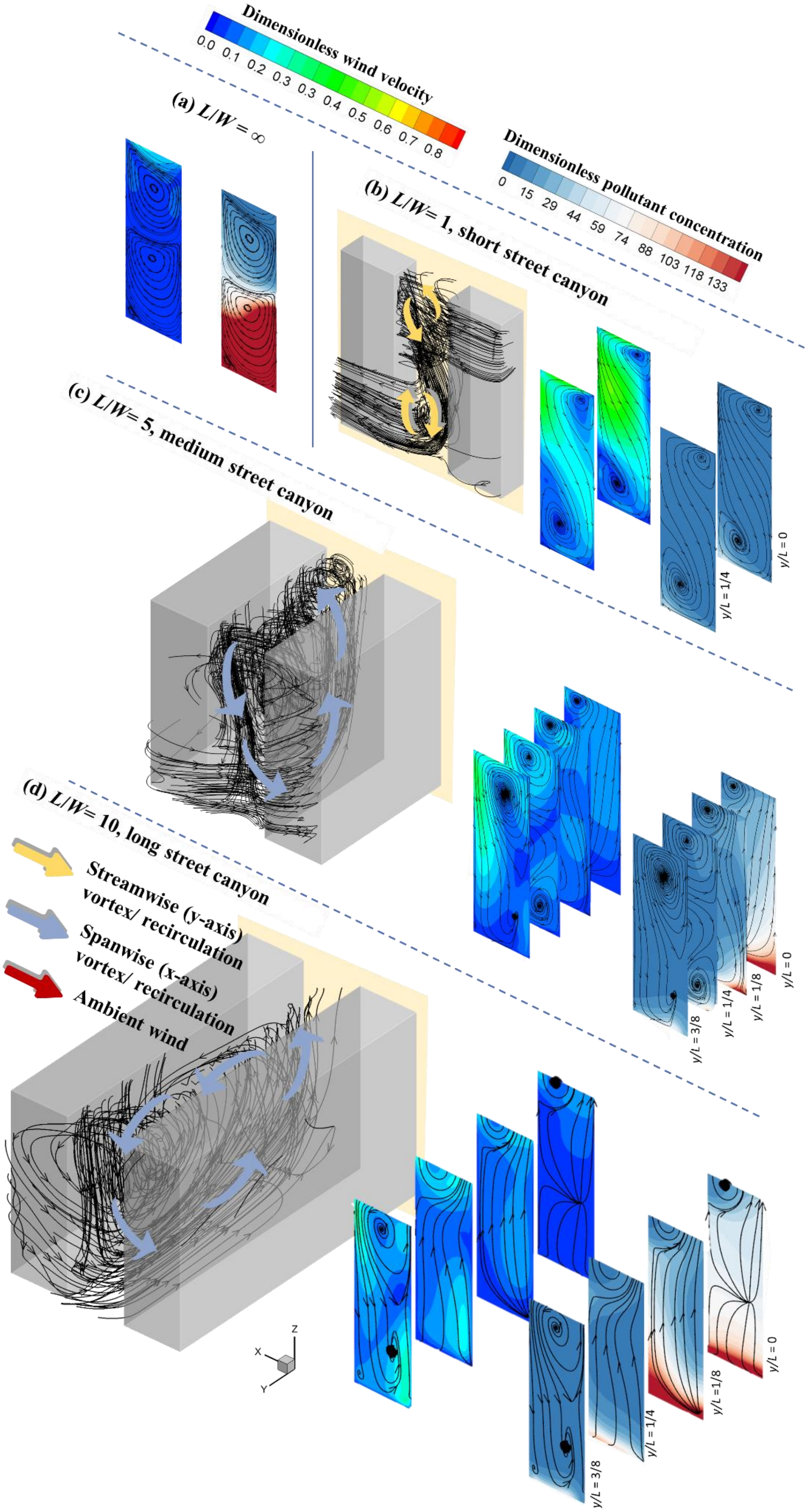

Dimensionless wind velocity
0.0 0.1 0.2 0.3 0.3 0.4 0.5 0.6 0.7 0.8
Dimensionless pollutant concentration
0 15 29 44 59 74 88 103 118 133
(a) L/W = ∞
(b) L/W= 1, short street canyon
y/L = 1/4
y/L = 0
(c) L/W= 5, medium street canyon
y/L = 3/8
y/L = 1/4
y/L = 1/8
y/L = 0
(d) L/W= 10, long street canyon
Streamwise (y-axis) vortex/ recirculation
Spanwise (x-axis) vortex/ recirculation
Ambient wind
y/L = 3/8
y/L = 1/4
y/L =1/8
y/L = 0

1

Fig. 12 Predicted pollutant concentration and wind velocity contours at different *x-z* cross-sections for the high-rise street canyons (*H/W*= 3) with various street lengths: (a) *L/W*= ∞, infinite-long street canyon, (b) *L/W*= 1, short street canyon, (c) *L/W*= 5, medium street canyon, and (d) *L/W*= 10, long street canyon.

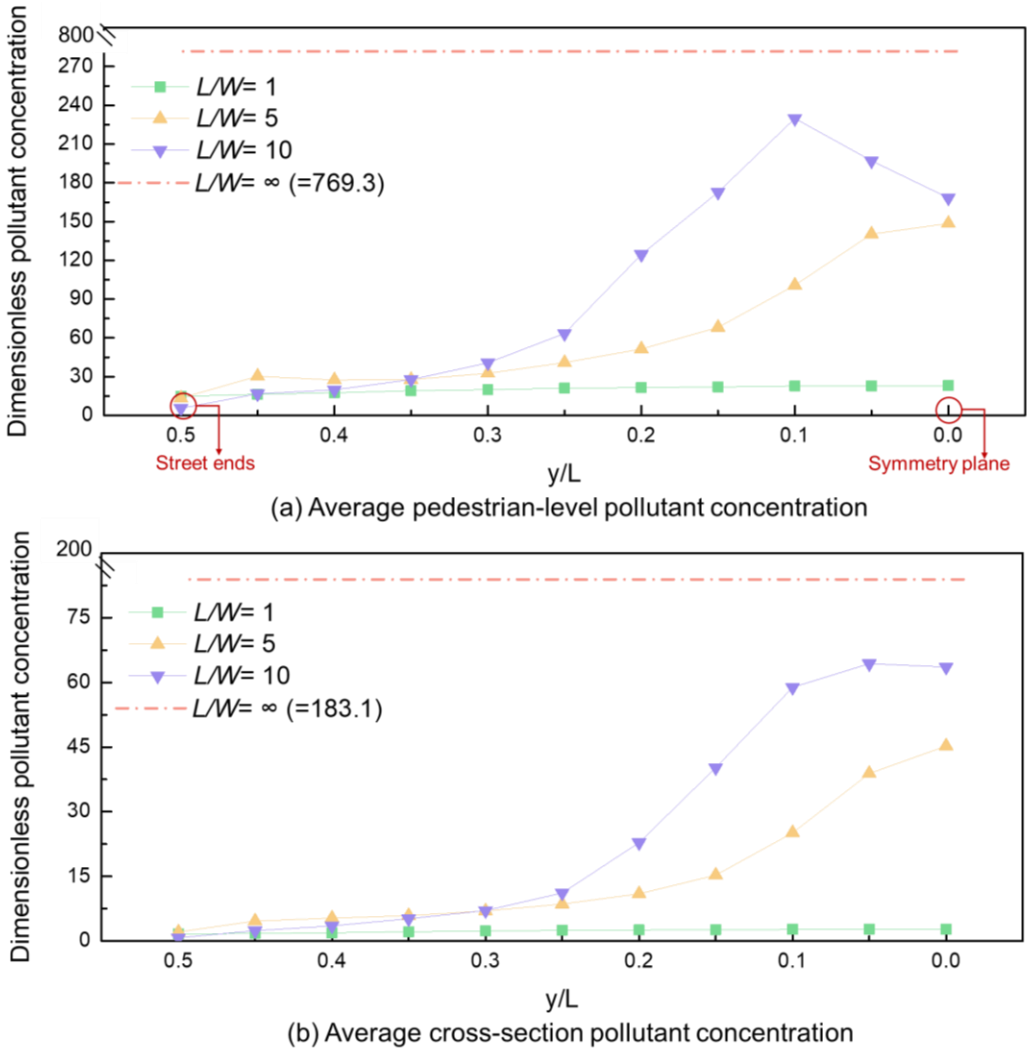

Fig. 13 Average pollutant concentration along half of the street length for the high-rise street canyon (*H/W*= 3) with various street lengths: (a) average pedestrian level pollutant concentration and (b) average cross-section pollutant concentration

5.2 Optimal urban design strategies for lateral entrainment

As discussed in the last section, the lateral entrainment can effectively improve the dilution potential of the pollutants inside the street canyon, especially for the deep canyons. In the low-rise medium street canyon (*H/W*= 1 and *L/W*= 5), the lateral entrainment caused the corner vortex at the street ends, and then, it contributed to the dilution of the pollutants near the ground level. In the high-rise street canyon (H/W= 3 and L/W= 5), the lateral entrainment had a more profound impact on the flow structure compared with the low-rise canyon, thus creating the x-axis recirculation in the lower space of the canyons. As discussed above, this x-axis recirculation can effectively improve the advective transport of the pollutants in the lower space. In summary, it might be useful to further improve the dilution potential of the pollutants by enhancing the intensity of the corner vortex in the low-rise street canyon or the x-axis recirculation in the high-rise street canyon. Therefore, three attempts have been made to enhance the influence of the lateral entrainments, i.e., the corner-trim of the downwind building, the short upwind building, and the lower height at the ends of the upwind building. In this section, the low-rise (H/W= 1) and high-rise (H/W= 3) canyons with the medium-long street (L/W=5) were considered to be the base cases to enhance the improvement on the pollutant concentration reduction. Also, the influence of dimensions of the corner-trim of downwind building D_{trim}, intended length of upwind building $L_{intended}$, and reduced height of upwind building $H_{reduced}$ has been examined in Fig. A4 to A6. It is suggested that even the relatively minor optimal design can effectively improve the ventilation and the potential of pollutant dilution inside street canyons. As length limits, only the cases of D_{trim} = 0.5 W, $L_{intended}$ = 0.5 W, and $H_{reduced}$ = 0.5 H were discussed in detail.

5.2.1 Design I: Corner-trim of the downwind building

The first attempt is to trim the corner of the downwind building, thus creating a "venturi effect" at the street ends. The dimensions of the trimmed corner are shown in Fig. 14 (a). A comparison of the results of the corner-trim and base cases in the low-rise street canyon is also presented. Notably, the maximum pedestrian level dimensionless wind velocity increased by approximately 0.2, although the flow structure changed only slightly. Hence, as illustrated in Fig. 14 (a), the concentration decreased in most of the canyons. This corner-trim design also significantly reduced the highest concentration of the base case in the canyon center region by up to almost 36% (Fig. 15(a)). On the other hand, in the vertical direction, this design also caused a significant reduction in the leeward side (leeward side P_IF reduced by almost 11%, Fig. 15(b)) since this design significantly enhanced the vertical ventilation on this side. Also, it slightly led to slightly lower windward *P_IF* by about 30- 100.

As seen in Fig. 14 (b), the corner-trim design had more significant implications for the reduction of the concentration in the high-rise case (*H*/*W*= 3). The “venturi effect” at the street ends caused a strong inward channeling flow toward the symmetry plane. Further, the intensity of the *x*-axis recirculation was also enhanced. The pedestrian level dimensionless wind velocity increased substantially by 0.5 (Fig. 14 (b)). Consequently, the pedestrian level concentration decreased in most of the canyons as a result (Fig. 14 (b)). At the same time, as shown in Fig. 14 (b), the base case had a higher concentration at both the street ends and symmetry plane. This corner-trim design can effectively reduce the pollutant concentration in these two regions (by up to almost 63%) (Fig. 14 (b) and Fig. 15 (a)). Additionally, as shown in Fig. 15 (c), the lower-story residents (level 2 to level 6) suffered high *P_IF* in the base case. The corner-trim design relieved this situation and effectively reduced leeward *P_IF* by up to 78% for the lower-story residents, although it slightly increased windward *P_IF* by 80-150.

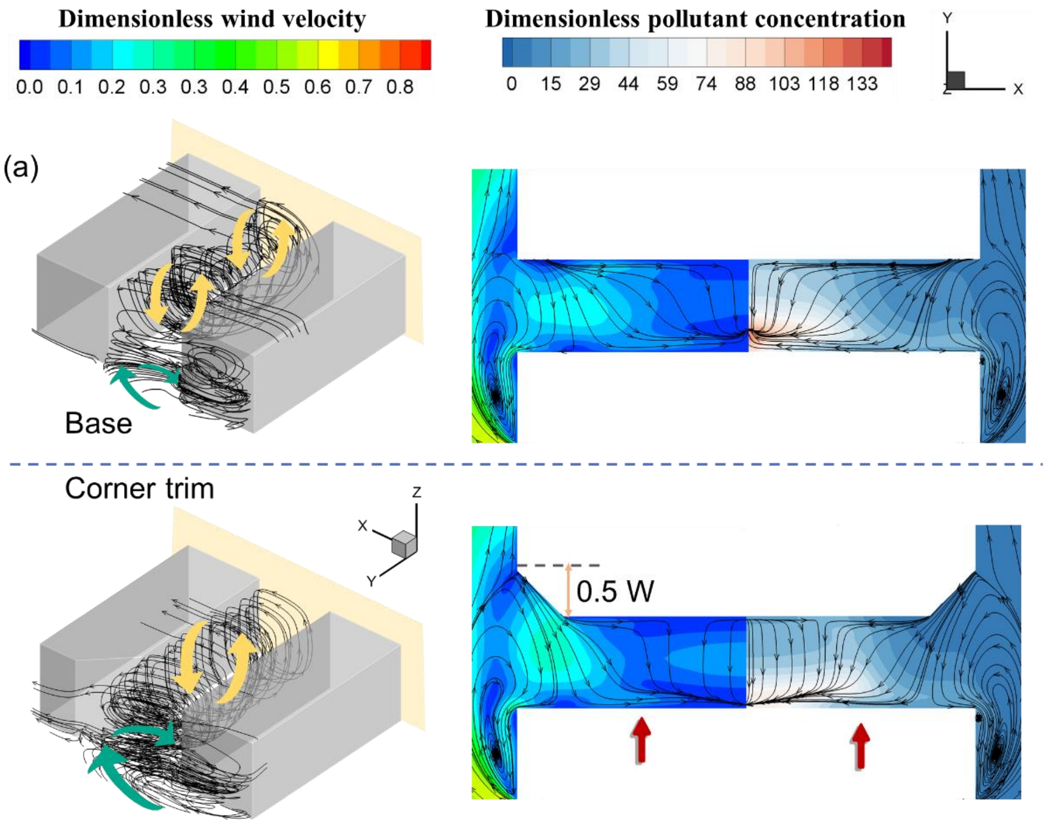

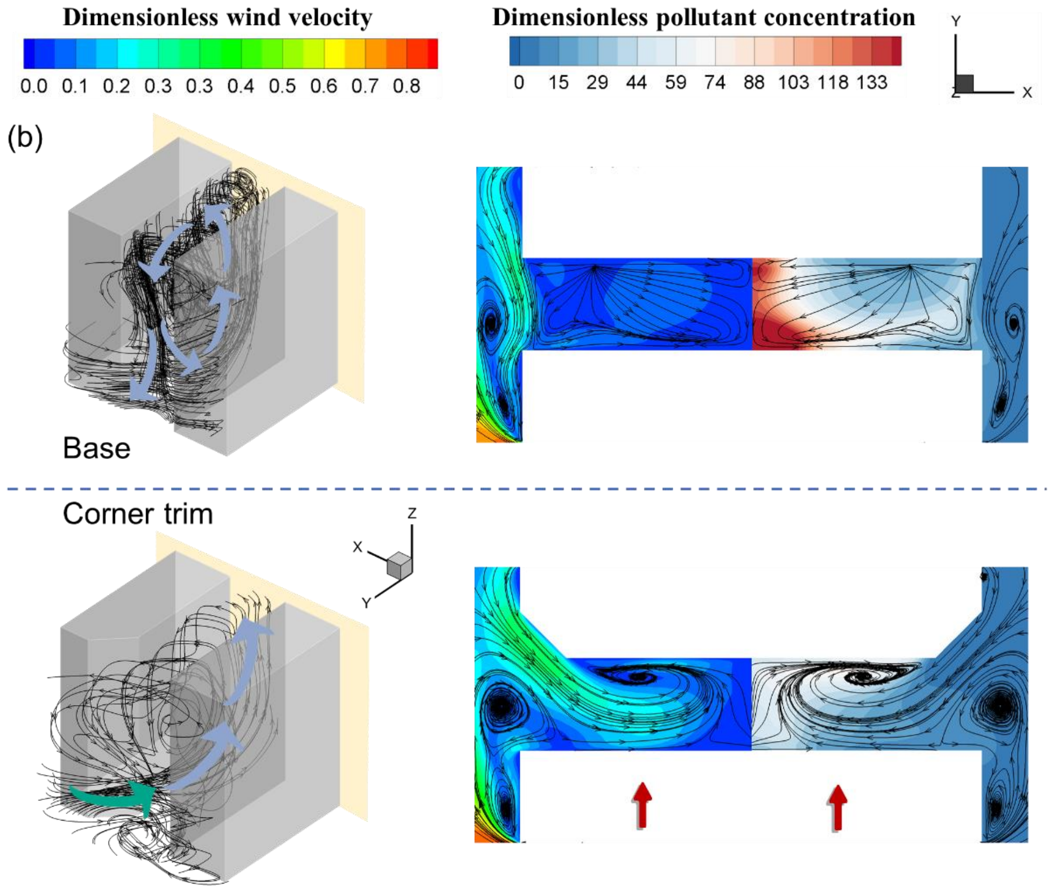

Fig. 14 Cross-comparison of the pollutant concentration at the pedestrian level between the base case and the corner-cut design case: (a) low-rise street canyon and (b) high-rise street canyon

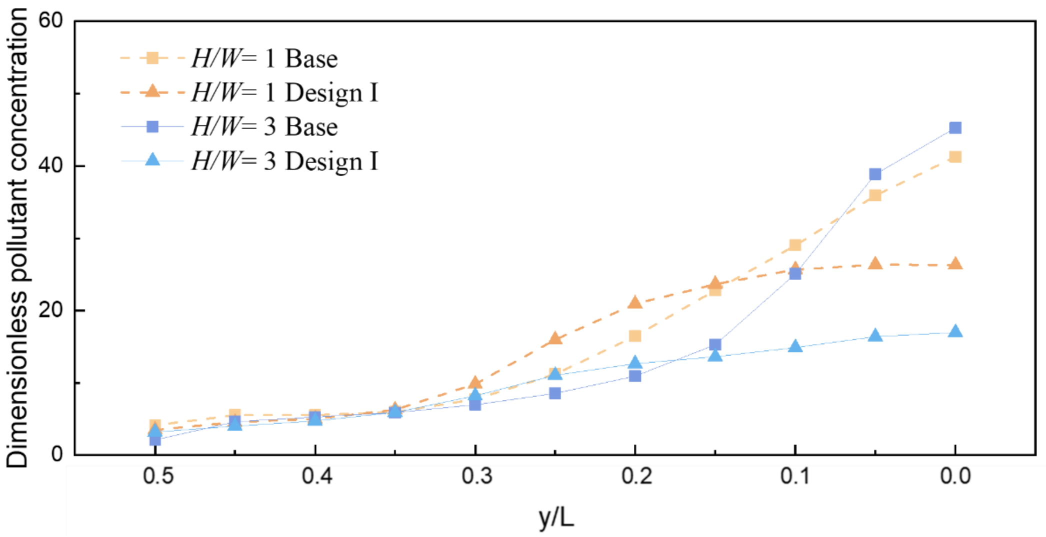

(a)Average cross-section pollutant concentration along the street length

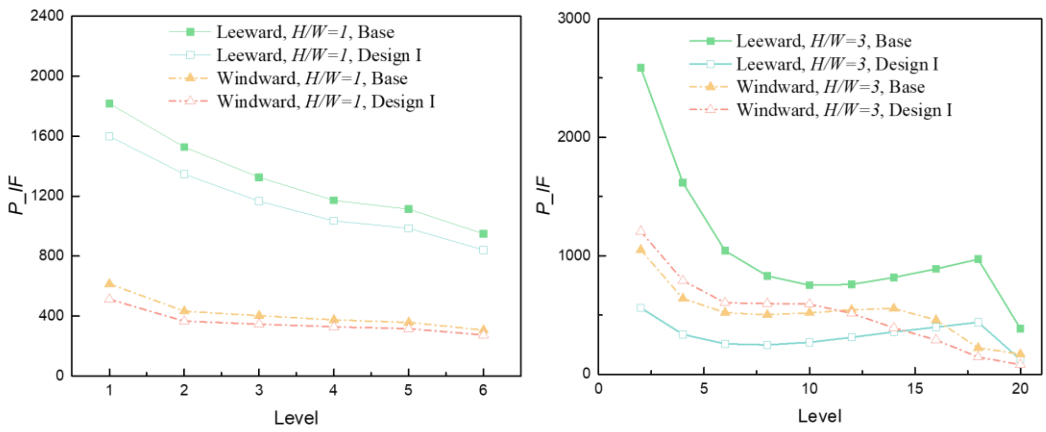

(b) *P_IF*, low-rise street canyon (c) *P_IF*, high-rise street canyon

Fig. 15 Cross-comparison of the pollutant concentration and personal intake fraction *P_IF* along the street length between the base case and corner-trim design case: (a) Average cross-section pollutant concentration along the street length, (b) *P_IF*, low-rise street canyon, and (c) *P_IF*, high-rise street canyon

5.2.2 Design II: Short upwind building

To enhance the influence of the lateral entrainment, the second attempt is to shorten the length of the upwind building by 1/2 *W*. Upon shortening the upwind building of the low-rise street canyon, as seen in the 3D streamlines of Fig. 16 (a), the lateral incoming wind flowed over the side of the upwind building, and it hit the windward surface of the downwind building. Then, the incoming wind flowed toward the symmetry plane, hence leading to a considerable increase in the dimensionless wind velocity at the pedestrian level (by up to 0.3). Correspondingly, the pedestrian level concentration was reduced significantly, especially in the canyon center region. In addition, as evidently shown in Fig. 17 (a), there was a large decrease in the cross-section pollutant concentration from y/L= 0.35 to 0 (by up to 45%). In addition, this design substantially reduced both leeward and windward *P_IF* from level 1 to level 6 (up to 49%) (Fig. 17(b)).

For the high-rise street canyon (H/W=3) with the short upwind building, as Fig. 16 (b) shows, the lateral incoming wind also hit the ends of the windward surface of the downwind building, and then, it enhanced the flow intensity of the *x*-axis recirculation. Therefore, there existed a strong upward airflow at the symmetry plane and a strong outward airflow at the pedestrian level (Fig. 16 (b)). The pedestrian level dimensionless wind velocity was remarkably improved (by up to 0.2). As a result, the accumulated pollutants in the canyon center region can easily escape from the street canyon across the street lateral boundaries. As shown in Fig. 17 (a), the concentration reduced in almost all of the street's length, especially in the canyon center region (by up to 76%). Additionally, by enhancing the intensity of the *x*-axis recirculation, this design appreciably reduced the windward *P_IF* by up to 44- 69% and the leeward *P_IF* by 71-81%, especially for the lower-story residents, who were always suffering the worst air quality.

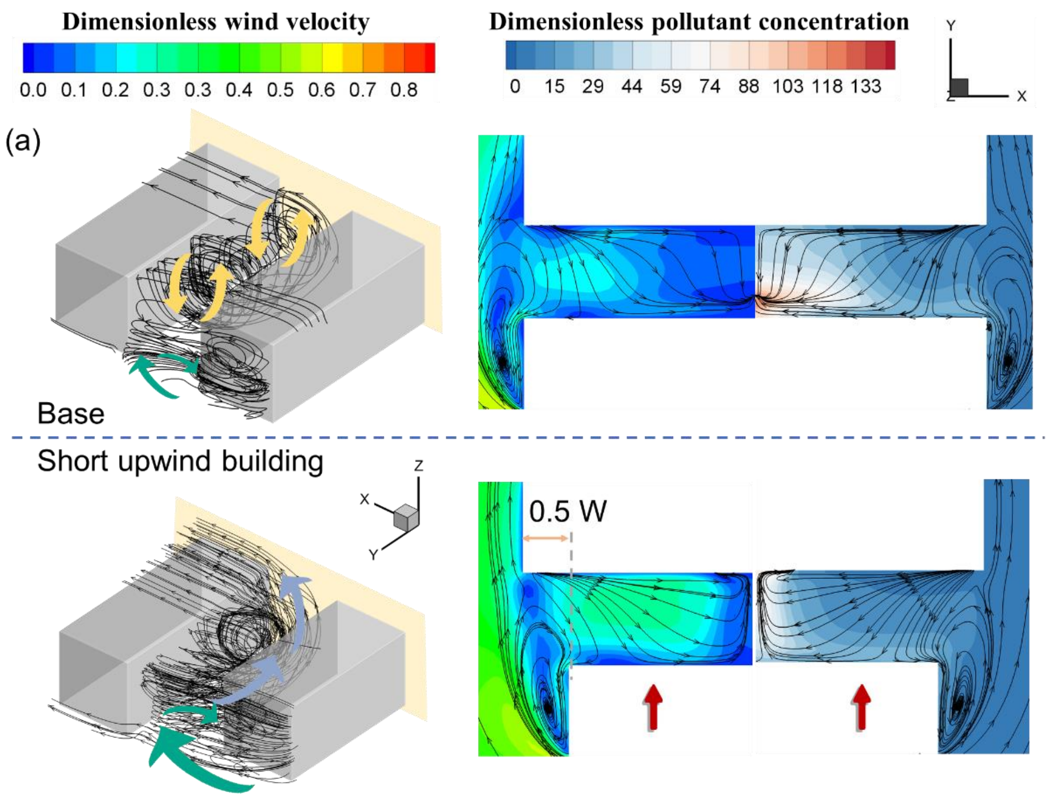

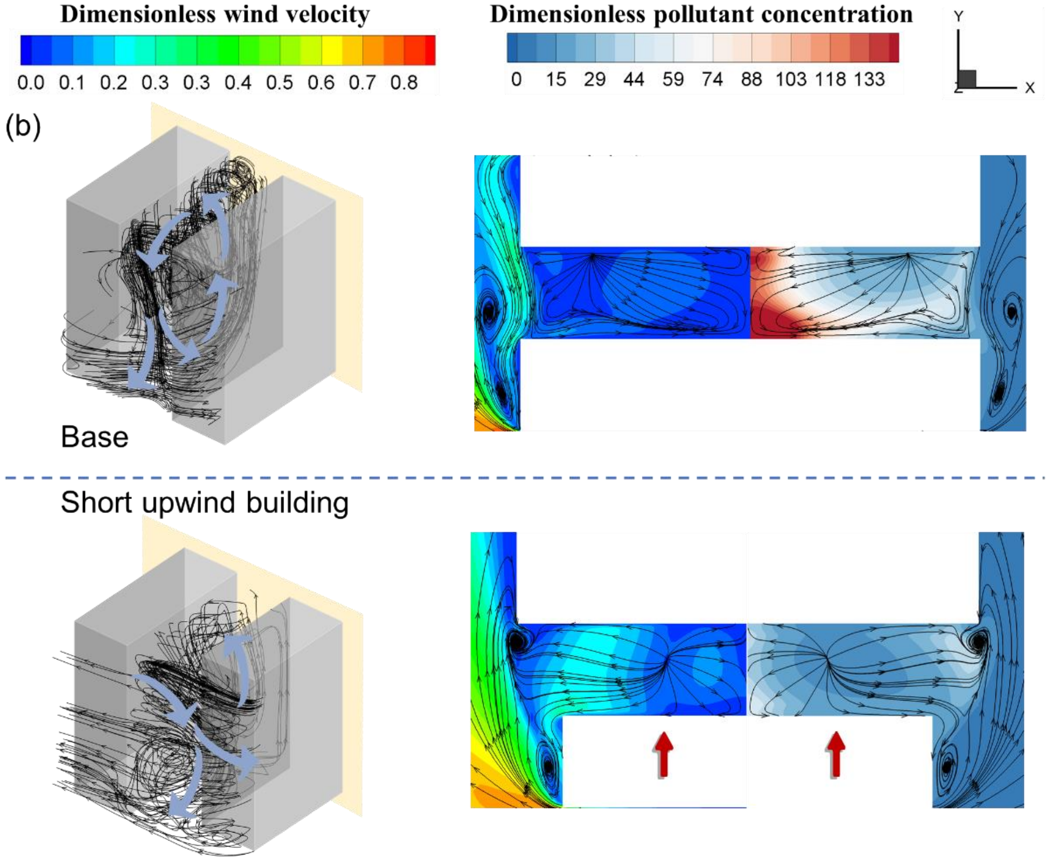

Fig. 16 Cross-comparison of the pollutant concentration at the pedestrian level between the base case and design II case: (a) low-rise street canyon and (b) high-rise street canyon

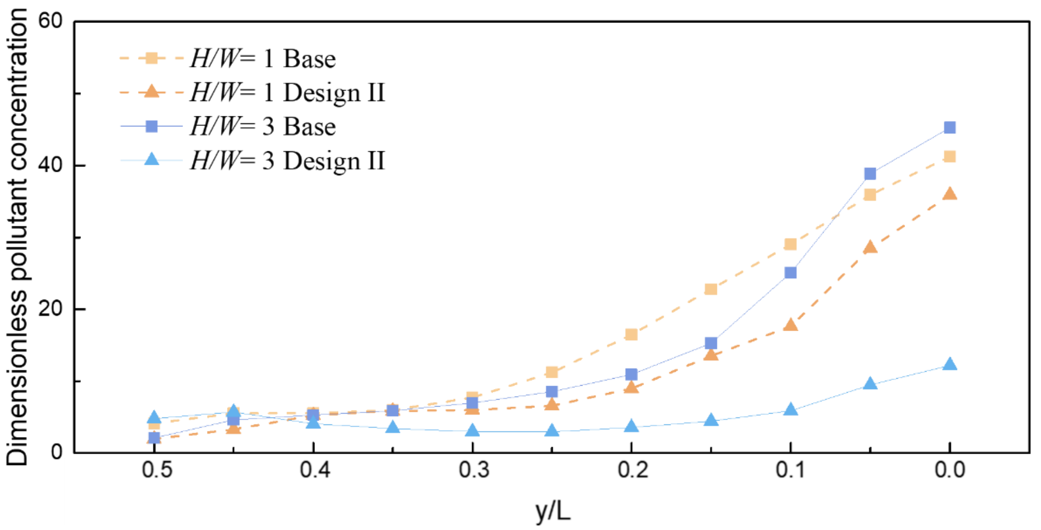

(a) Average cross-section pollutant concentration along the street length

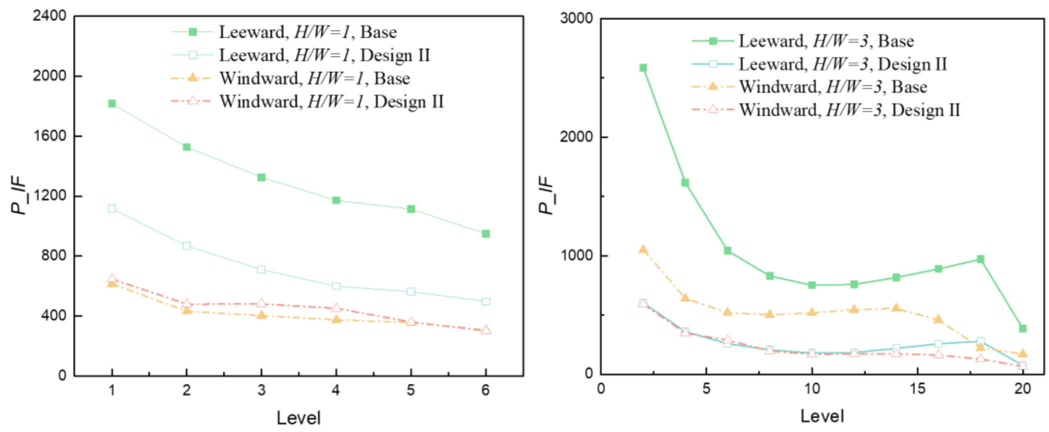

(b) *P_IF*, low-rise street canyon (c) *P_IF*, high-rise street canyon

Fig. 17 Cross-comparison of the pollutant concentration and personal intake fraction *P_IF* along the street length between the base case and design II case: (a) Average cross-section pollutant concentration along the street length, (b) *P_IF*, low-rise street canyon, and (c) *P_IF*, high-rise street canyon.

5.2.3 Design III: Lower height at the ends of the upwind building

As discussed in section 5.2.2, design II successfully introduced the lateral incoming flow into the street canyon from the street ends, hence increasing the flow strength of the *x*-axis recirculation and reducing the pollutant concentration. However, design II will be at the cost of a lower building coverage ratio. Thus, the third attempt is to explore whether only lowering the building height at the ends of the upwind building can also improve the ventilation in the same way (Fig. 18(a) and (b)).

For the low-rise street canyon with design III (the indented length = 1/2 *W* and the reduced height = 0.5 *H*), as seen in the 3D streamlines of Fig. 18 (a), the pedestrian level wind velocity was markedly improved by introducing fresh air from the upper part of the lateral street boundaries, the same as in design II. Therefore, the cross-section pollutant concentration also reduced substantially from y/L= 0.4 to 0 (by up to 34%) (Fig. 19 (a)). Clearly, for the low-rise canyons, the reduction in the pedestrian level concentration due to design III was only slightly lower than in the design II counterpart. In terms of *P_IF* (Fig. 17(b)), this design also reduced leeward *P_IF* from level 1 to level 6 (up to 39%), but the windward *P_IF* had little change.

For the high-rise street canyon with design III (the indented length = 1/2 *W* and the reduced height = 1/3 H), similar to design II, the wind velocity was also improved (Fig. 18 (b)), although the increment in the wind velocity is less than that of design II (Fig. 16 (b)). Therefore, as shown in Fig. 19 (a), there was a considerable decrease in the pedestrian level concentration along the street length, especially in the canyon center region (by up to 71%). Furthermore, the *P_IF* noticeably declined at both the leeward side (by 55-73%) and the windward side (by up to 56-73%).

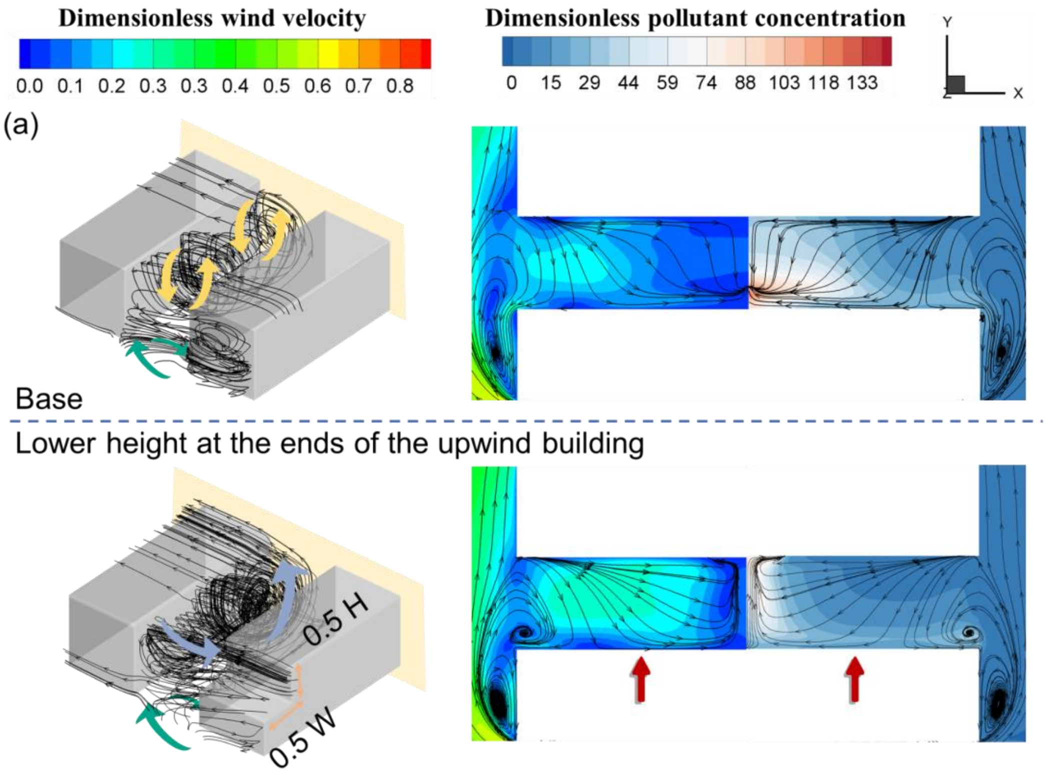

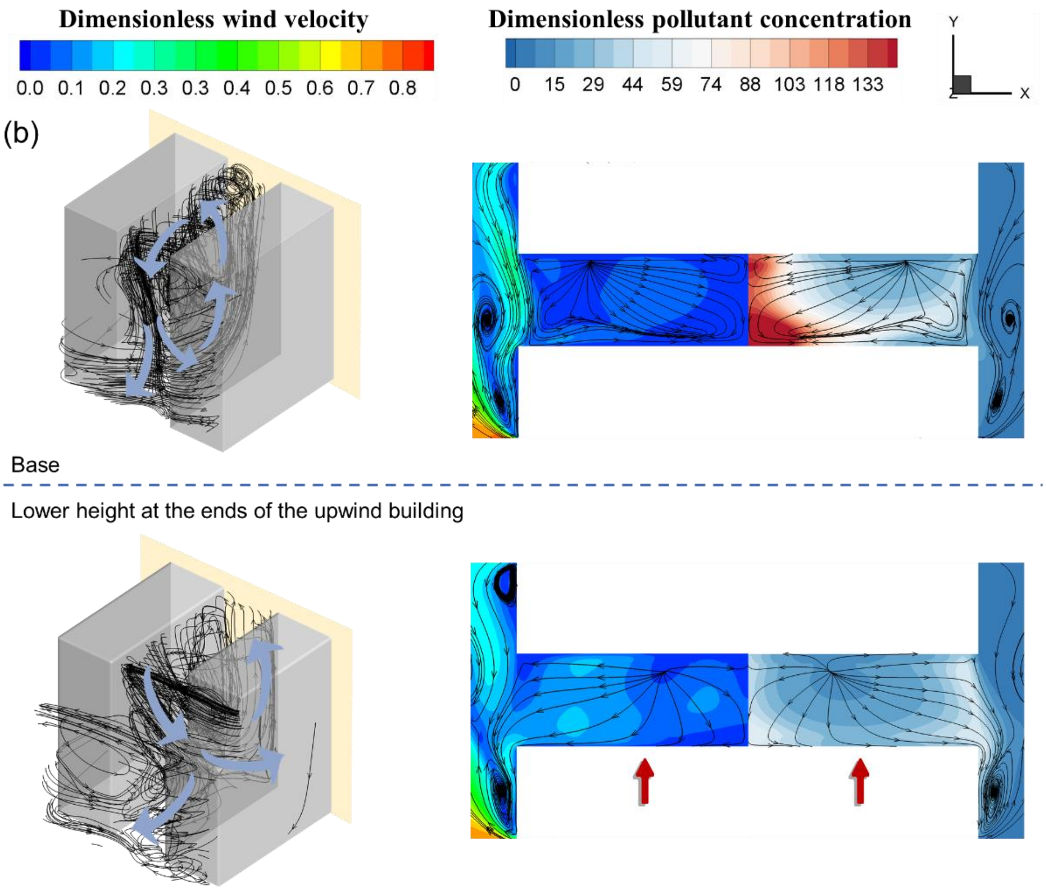

Fig. 18 Cross-comparison of the pollutant concentration at the pedestrian level between the base case and design III case:

(a) low-rise street canyon and (b) high-rise street canyon

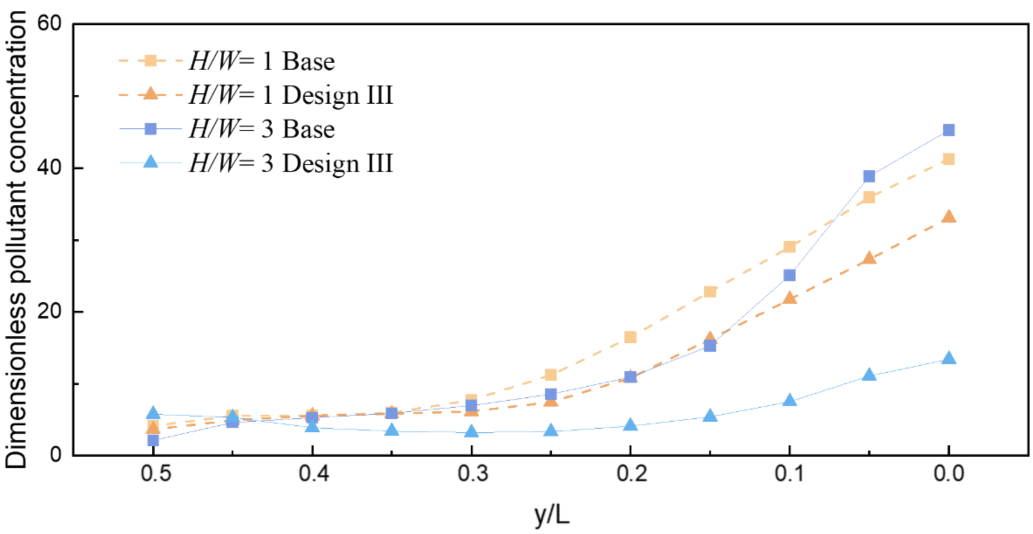

(a) Average cross-section pollutant concentration along the street length

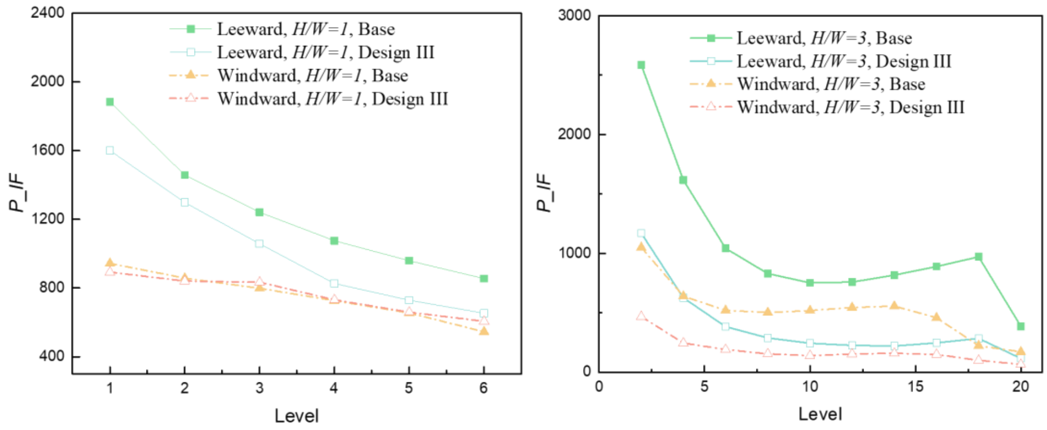

(b) *P_IF*, low-rise street canyon (c) *P_IF*, high-rise street canyon

Fig. 19 Cross-comparison of the pollutant concentration and personal intake fraction *P_IF* along the street length between the base case and design III case: (a) Average cross-section pollutant concentration along the street length, (b) *P_IF*, low-rise street canyon, and (c) *P_IF*, high-rise street canyon

6. Conclusions and Limitations

6.1 Conclusions

This paper has presented numerical simulations with Computational Fluid Dynamics (CFD) to investigate the influence of the lateral entrainment on the pollutant concentration within the street canyons based on eight 3D street canyons with different aspect ratios of building height and length to street width (H/W and L/W) under the perpendicular wind. The simulations were based on grid-sensitivity analysis and validation of the CFD results from the literature. Based on the CFD results, the importance of the lateral entrainment was confirmed. Further, three designs were proposed to improve air quality by enhancing the influence of lateral entrainment. The major results are summarized as follows:

(1) In a low-rise street canyon, the flow structure was mainly dominated by the top entrainment. The lateral entrainment slightly altered the flow, except for the appearance of the corner vortex and the inward channeling flow near the ground level. Thus, the positive effect of the lateral entrainment on the pollutant concentration was limited (approximately 2.5 times the street width from the street end). For example, the lateral entrainment can significantly reduce both

the cross-section and pedestrian level pollutant concentrations of the short and medium canyon by up to 78%. However, for the long canyon, these two concentrations declined only for the outer half of the street in the length direction due to the lateral entrainment.

(2) In a high-rise street canyon, the top entrainment caused only one canyon vortex (the axis was parallel to the street length) in the upper space. In contrast, the lateral entrainment dominated the lower space by the two symmetric vortices/recirculation with an axis perpendicular to the street length. Thus, the pollutant concentrations markedly decreased by up to almost 99% for the short, medium, and long street canyons, due to the lateral entrainment, compared with the case of only considering the top entrainment.

(3) All of the three optimal designs were considerably useful in reducing the pollutant concentration by enhancing the lateral entrainment, especially for the high-rise street canyons. First, the corner-trim of the downwind building created a "venturi effect" at the street ends, thus significantly reducing the cross-section concentration in most regions of the street canyon (by up to almost 36% and 63% for the low-rise and high-rise canyons) and the personal intake fraction *P_IF* (by up to almost 11% and 78% for the low-rise and high-rise canyons). Second, the short upwind building notably introduced the incoming wind impinging at the ends of the downwind building; thus, the cross-section concentration greatly decreased in both the low-rise canyons (by up to 45%) and the high-rise canyons (by up to 76%). In addition, it reduced the *P_IF* of the low-rise canyons by up to 49%, and the *P_IF* of the high-rise canyons by up to 81%. Third, the lower height at the ends of the upwind building also introduced fresh air in the same way as in the setup of the short upwind building, alleviating the cost of a lower building coverage ratio (the design III is less expensive than the design II). The reduction in the concentrations caused by this design was just slightly lower than the setup of a short upwind building.

By discussing those results, two suggestions can be proposed for sustainable street design to reduce pollutant concentration inside street canyons. First, the importance of lateral entrainment should not be neglected, especially for the high-rise street canyon. Therefore, less blockage should be achieved at the street ends. In other words, at the street ends, large-size advertisement boards [57] should not be installed or trees with large-size canopy and high leaf area density [58,59] should not be planted. Second, to utilize the lateral entrainment to improve the ventilation within street canyons, it might be feasible to create a corner trim of downwind buildings at the street ends. Also, the upwind buildings of street canyon should be shorter than the downwind buildings.

6.2 Limitations

Despite the obtained findings, the present study had several limitations. First, only one boundary condition (perpendicular wind with constant wind speed) was considered, but in actual practice, ambient wind could flow into the urban configuration from all directions with different wind speeds. It is expected that the minor variation of wind direction might significantly alter the lateral entrainment. Second, this study is limited to isothermal conditions. In effect, the buoyancy effect due to temperature differences between heated building surfaces/ground and ambient air should not be ignored, which is an essential driving force for natural ventilation, especially when the wind is relatively weak. For instance, the heated leeward surface by solar radiation can cause a stronger upward airflow in the center of the canyon [15], which might influence lateral entrainment. Third, this study only used a generic street canyon configuration. However, real urban areas consist of irregular arrangements of buildings of various heights. Irregular arrangements of buildings may modify the influence of lateral entrainment. Finally, only the RANS model and the RNG k-ε model were used to predict the urban wind flow under steady-state conditions. It is known that the RANS models provide effective time-averaged flow solutions. The dispersion contribution of transient fluctuations, however, are compromised. Additionally, even with a lower turbulent Schmidt number (= 0.4) set to account for the underestimation of the turbulent mass diffusion from the RANS model, the accumulation of pollutants near the ground level could be overestimated, especially for the high-rise street canyon. In contrast, the large eddy simulation (LES) model can provide more accurate results due to its better capture of flow intermittencies and separations around the street canyon. However, due to the high computation cost and challenges in selecting sub-grid scale models with appropriate boundary conditions by using the LES model, many studies still select the RANS approach instead [58]. In this regard, a more accurate RANS turbulence model, such as Shear-Stress Transport (SST) k-ω model or Reynolds Stress Model (RSM), should be adopted to evaluate the influence of lateral entrainment under unsteady-state conditions. Generally, all these factors could influence the lateral entrainment investigated in this study, and this will be explored in our future studies.

REFERENCE

[1] S. Grimmond, Urbanization and global environmental change: local effects of urban warming, Geogr. J. 173 (2007) 83–88.

[2] R. Rückerl, A. Schneider, S. Breitner, J. Cyrys, A. Peters, Health effects of particulate air pollution: a review of epidemiological evidence, Inhal. Toxicol. 23 (2011) 555–592.

[3] Y. Xia, D. Guan, X. Jiang, L. Peng, H. Schroeder, Q. Zhang, Assessment of socioeconomic costs to China's air pollution, Atmos. Environ. 139 (2016) 147–156. doi:https://doi.org/10.1016/j.atmosenv.2016.05.036.

[4] A.-S. Yang, Y.-H. Juan, C.-Y. Wen, C.-J. Chang, Numerical simulation of cooling effect of vegetation enhancement in a subtropical urban park, Appl. Energy. 192 (2017) 178–200. doi:https://doi.org/10.1016/j.apenergy.2017.01.079.

[5] A.-S. Yang, C.-Y. Wen, Y.-H. Juan, Y.-M. Su, J.-H. Wu, Using the central ventilation shaft design within public buildings for natural aeration enhancement, Appl. Therm. Eng. 70 (2014) 219–230. doi:https://doi.org/10.1016/j.applthermaleng.2014.05.017.

[6] P. Edussuriya, A. Chan, A. Ye, Urban morphology and air quality in dense residential environments in Hong Kong. Part I: District-level analysis, Atmos. Environ. 45 (2011) 4789–4803. doi:https://doi.org/10.1016/j.atmosenv.2009.07.061.

[7] Z. Li, T. Ming, S. Liu, C. Peng, R. de Richter, W. Li, H. Zhang, C.-Y. Wen, Review on pollutant dispersion in urban areas-part A: Effects of mechanical factors and urban morphology, Build. Environ. (2020) 107534.

[8] S.-J. Mei, J.-T. Hu, D. Liu, F.-Y. Zhao, Y. Li, H.-Q. Wang, Airborne pollutant dilution inside the deep street canyons subjecting to thermal buoyancy driven flows: Effects of representative urban skylines, Build. Environ. 149 (2019) 592–606. doi:https://doi.org/10.1016/j.buildenv.2018.12.050.

[9] W.C. Cheng, C.-H. Liu, D.Y.C. Leung, Computational formulation for the evaluation of street canyon ventilation and pollutant removal performance, Atmos. Environ. 42 (2008) 9041–9051.

[10] D. Marucci, M. Carpentieri, Effect of local and upwind stratification on flow and dispersion inside and above a bi-dimensional street canyon, Build. Environ. 156 (2019) 74–88.

[11] V.D. Assimakopoulos, H.M. ApSimon, N. Moussiopoulos, A numerical study of atmospheric pollutant dispersion in different two-dimensional street canyon configurations, Atmos. Environ. 37 (2003) 4037–4049.

[12] S.E. Belcher, Mixing and transport in urban areas, Philos. Trans. R. Soc. A Math. Phys. Eng. Sci. 363 (2005) 2947–2968.

[13] F. Caton, R.E. Britter, S. Dalziel, Dispersion mechanisms in a street canyon, Atmos. Environ. 37 (2003) 693–702.

[14] A. Di Bernardino, P. Monti, G. Leuzzi, G. Querzoli, Pollutant fluxes in two-dimensional street canyons, Urban Clim. 24 (2018) 80–93.

[15] Z. Li, H. Zhang, C.-Y. Wen, A.-S. Yang, Y.-H. Juan, Effects of height-asymmetric street canyon configurations on outdoor air temperature and air quality, Build. Environ. (2020) 107195.

[16] Z. Li, H. Zhang, C.-Y. Wen, A.-S. Yang, Y.-H. Juan, Effects of frontal area density on outdoor thermal comfort and air quality, Build. Environ. 180 (2020) 107028. doi:https://doi.org/10.1016/j.buildenv.2020.107028.

[17] W.G. Hoydysh, W.F. Dabberdt, Kinematics and dispersion characteristics of flows in asymmetric street canyons, Atmos. Environ. 22 (1988) 2677–2689.

[18] C. Gromke, B. Ruck, Influence of trees on the dispersion of pollutants in an urban street canyon—experimental investigation of the flow and concentration field, Atmos. Environ. 41 (2007) 3287–3302.

[19] L.J. Hunter, G.T. Johnson, I.D. Watson, An investigation of three-dimensional characteristics of flow regimes within the urban canyon, Atmos. Environ. Part B. Urban Atmos. 26 (1992) 425–432. doi:https://doi.org/10.1016/0957-1272(92)90049-X.

[20] B.M. Leitl, R.N. Meroney, Car exhaust dispersion in a street canyon. Numerical critique of a wind tunnel experiment, J. Wind Eng. Ind. Aerodyn. 67 (1997) 293–304.

[21] C. Gromke, B. Ruck, Pollutant concentrations in street canyons of different aspect ratio with avenues of trees for various wind directions, Boundary-Layer Meteorol. 144 (2012) 41–64.

[22] C. Gromke, N. Jamarkattel, B. Ruck, Influence of roadside hedgerows on air quality in urban street canyons, Atmos. Environ. 139 (2016) 75–86. doi:https://doi.org/10.1016/j.atmosenv.2016.05.014.

[23] M.Y. Tsai, K.S. Chen, Measurements and three-dimensional modeling of air pollutant dispersion in an Urban Street Canyon, Atmos. Environ. 38 (2004) 5911–5924.

[24] L. Soulhac, V. Garbero, P. Salizzoni, P. Mejean, R.J. Perkins, Flow and dispersion in street intersections, Atmos. Environ. 43 (2009) 2981–2996.

[25] S. Vardoulakis, B.E.A. Fisher, K. Pericleous, N. Gonzalez-Flesca, Modelling air quality in street canyons: a review, Atmos. Environ. 37 (2003) 155–182. doi:https://doi.org/10.1016/S1352-2310(02)00857-9.

[26] S.-J. Mei, Z. Luo, F.-Y. Zhao, H.-Q. Wang, Street canyon ventilation and airborne pollutant dispersion: 2-D versus 3-D CFD simulations, Sustain. Cities Soc. 50 (2019) 101700. doi:https://doi.org/10.1016/j.scs.2019.101700.

[27] Z. Li, T. Shi, Y. Wu, H. Zhang, Y.-H. Juan, T. Ming, N. Zhou, Effect of traffic tidal flow on pollutant dispersion in various street canyons and corresponding mitigation strategies, Energy Built Environ. 1 (2020) 242–253. doi:https://doi.org/10.1016/j.enbenv.2020.02.002.

[28] Y. Du, C.M. Mak, Y. Li, A multi-stage optimization of pedestrian level wind environment and thermal comfort with lift-up design in ideal urban canyons, Sustain. Cities Soc. 46 (2019) 101424. doi:https://doi.org/10.1016/j.scs.2019.101424.

[29] Y.-H. Juan, A.-S. Yang, C.-Y. Wen, Y.-T. Lee, P.-C. Wang, Optimization procedures for enhancement of city breathability using arcade design in a realistic high-rise urban area, Build. Environ. 121 (2017) 247–261. doi:https://doi.org/10.1016/j.buildenv.2017.05.035.

[30] C.-Y. Wen, Y.-H. Juan, A.-S. Yang, Enhancement of city breathability with half open spaces in ideal urban street canyons, Build. Environ. 112 (2017) 322–336.

doi:https://doi.org/10.1016/j.buildenv.2016.11.048.
[31] J.I. Perén, T. van Hooff, B.C.C. Leite, B. Blocken, CFD simulation of wind-driven upward cross ventilation and its enhancement in long buildings: Impact of single-span versus double-span leeward sawtooth roof and opening ratio, Build. Environ. 96 (2016) 142–156.
[32] C. Gromke, B. Ruck, On the impact of trees on dispersion processes of traffic emissions in street canyons, Boundary-Layer Meteorol. 131 (2009) 19–34.
[33] C. Gromke, CODASC: a database for the validation of street canyon dispersion models, in: 15th Int. Conf. Harmon. within Atmos. Dispers. Model. Regul. Purp., 2013.
[34] T.R. Oke, Street design and urban canopy layer climate, Energy Build. 11 (1988) 103–113.
[35] Y. Tominaga, A. Mochida, R. Yoshie, H. Kataoka, T. Nozu, M. Yoshikawa, T. Shirasawa, AIJ guidelines for practical applications of CFD to pedestrian wind environment around buildings, J. Wind Eng. Ind. Aerodyn. 96 (2008) 1749–1761. doi:https://doi.org/10.1016/j.jweia.2008.02.058.
[36] Y. Tominaga, T. Stathopoulos, Turbulent Schmidt numbers for CFD analysis with various types of flowfield, Atmos. Environ. 41 (2007) 8091–8099. doi:https://doi.org/10.1016/j.atmosenv.2007.06.054.
[37] J. Hang, Y. Li, R. Buccolieri, M. Sandberg, S. Di Sabatino, On the contribution of mean flow and turbulence to city breathability: the case of long streets with tall buildings, Sci. Total Environ. 416 (2012) 362–373.
[38] V. Yakhot, L.M. Smith, The renormalization group, the ε-expansion and derivation of turbulence models, J. Sci. Comput. 7 (1992) 35–61.
[39] J.-J. Kim, J.-J. Baik, A numerical study of the effects of ambient wind direction on flow and dispersion in urban street canyons using the RNG k–ε turbulence model, Atmos. Environ. 38 (2004) 3039–3048. doi:https://doi.org/10.1016/j.atmosenv.2004.02.047.
[40] J.-J. Kim, D.-Y. Kim, Effects of a building's density on flow in urban areas, Adv. Atmos. Sci. 26 (2009) 45–56.
[41] P.J. Richards, R.P. Hoxey, Appropriate boundary conditions for computational wind engineering models using the k-ε turbulence model, in: Comput. Wind Eng. 1, Elsevier, 1993: pp. 145–153.
[42] B.E. Launder, D.B. Spalding, The numerical computation of turbulent flows, in: Numer. Predict. Flow, Heat Transf. Turbul. Combust., Elsevier, 1983: pp. 96–116.
[43] T. Cebeci, P. Bradshaw, Momentum transfer in boundary layers, Hemi. (1977).
[44] B. Blocken, T. Stathopoulos, J. Carmeliet, CFD simulation of the atmospheric boundary layer: wall function problems, Atmos. Environ. 41 (2007) 238–252.
[45] W.-Y. Ng, C.-K. Chau, A modeling investigation of the impact of street and building configurations on personal air pollutant exposure in isolated deep urban canyons, Sci. Total Environ. 468–469 (2014) 429–448. doi:https://doi.org/10.1016/j.scitotenv.2013.08.077.
[46] A. Fluent, ANSYS fluent theory guide 15.0, Inc, Canonsburg, PA. (2013).
[47] T. Barth, D. Jespersen, The design and application of upwind schemes on unstructured meshes, in: 27th Aerosp. Sci. Meet., 1989: p. 366.
[48] P.J. Roache, Quantification of uncertainty in computational fluid dynamics, Annu. Rev. Fluid Mech. 29 (1997) 123–160.
[49] H. Schlichting, K. Gersten, Boundary-layer theory, Springer, 2016.
[50] R. Zhang, Y. Zhang, K.P. Lam, D.H. Archer, A prototype mesh generation tool for CFD simulations in architecture domain, Build. Environ. 45 (2010) 2253–2262.
[51] J. Hang, Z. Luo, X. Wang, L. He, B. Wang, W. Zhu, The influence of street layouts and viaduct settings on daily carbon monoxide exposure and intake fraction in idealized urban canyons, Environ. Pollut. 220

(2017) 72–86. doi:https://doi.org/10.1016/j.envpol.2016.09.024.
[52] D. Cui, X. Li, Y. Du, C.M. Mak, K. Kwok, Effects of envelope features on wind flow and pollutant exposure in street canyons, Build. Environ. 176 (2020) 106862. doi:https://doi.org/10.1016/j.buildenv.2020.106862.
[53] H. Yu, J. Thé, Validation and optimization of SST k-ω turbulence model for pollutant dispersion within a building array, Atmos. Environ. 145 (2016) 225–238.
[54] Y.-W. Zhang, Z.-L. Gu, S.-C. Lee, T.-M. Fu, K.-F. Ho, Numerical Simulation and In Situ Investigation of Fine Particle Dispersion in an Actual Deep Street Canyon in Hong Kong, Indoor Built Environ. 20 (2010) 206–216. doi:10.1177/1420326X10387694.
[55] T. Shi, T. Ming, Y. Wu, C. Peng, Y. Fang, R. de_Richter, The effect of exhaust emissions from a group of moving vehicles on pollutant dispersion in the street canyons, Build. Environ. 181 (2020) 107120. doi:https://doi.org/10.1016/j.buildenv.2020.107120.
[56] X. Xie, Z. Huang, J. Wang, Z. Xie, The impact of solar radiation and street layout on pollutant dispersion in street canyon, Build. Environ. 40 (2005) 201–212.
[57] Y. Lin, G. Chen, T. Chen, Z. Luo, C. Yuan, P. Gao, J. Hang, The influence of advertisement boards, street and source layouts on CO dispersion and building intake fraction in three-dimensional urban-like models, Build. Environ. 150 (2019) 297–321.
[58] H. Yang, T. Chen, Y. Lin, R. Buccolieri, M. Mattsson, M. Zhang, J. Hang, Q. Wang, Integrated impacts of tree planting and street aspect ratios on CO dispersion and personal exposure in full-scale street canyons, Build. Environ. 169 (2020) 106529. doi:https://doi.org/10.1016/j.buildenv.2019.106529.
[59] T. Chen, H. Yang, G. Chen, C.K.C. Lam, J. Hang, X. Wang, Y. Liu, H. Ling, Integrated impacts of tree planting and aspect ratios on thermal environment in street canyons by scaled outdoor experiments, Sci. Total Environ. (2020) 142920.

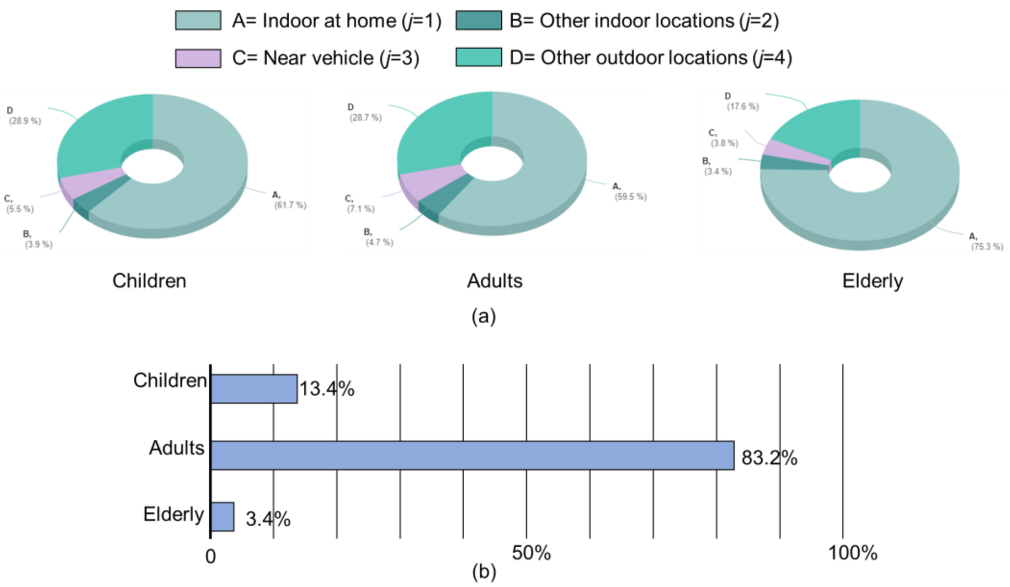

Fig. A1 (a) Time activity patterns for different age groups and microenvironments; and (b) demographic structure in Shenzhen, China[52].

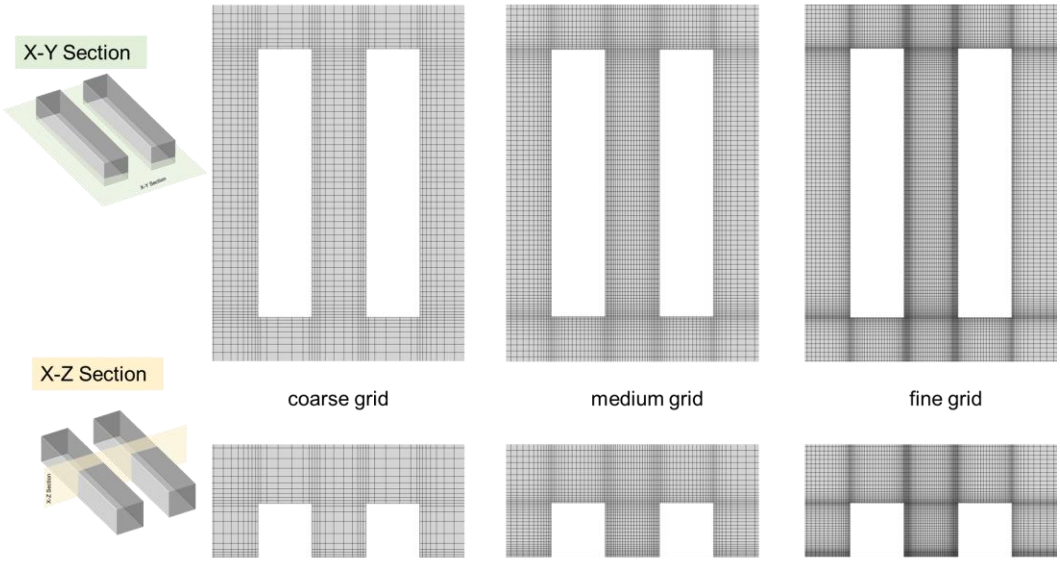

Fig. A2 Detailed information across the tested street canyon for all three grid sensitivity analysis cases

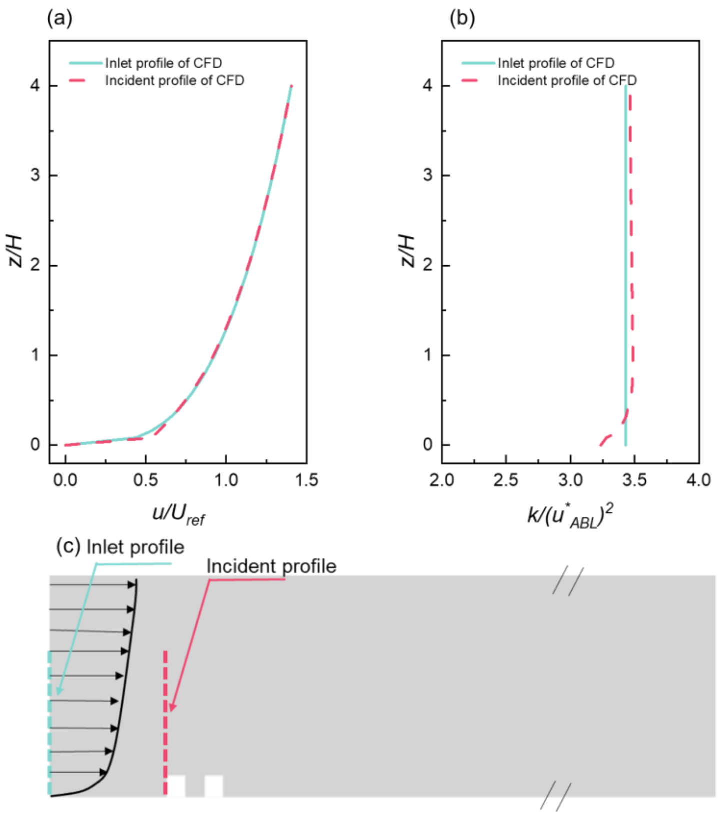

Fig. A3. (a) Comparison of inlet and incident dimensionless streamwise velocity (u/U_{ref}) profiles, (b) Comparison of inlet and incident dimensionless turbulence kinetic energy ($k/(u^{*}_{ABL})^2$) profiles, and (c) Schematic cross-section of the domain with location of inlet profile (x/H = 0) and incident profile (x/H = 5).

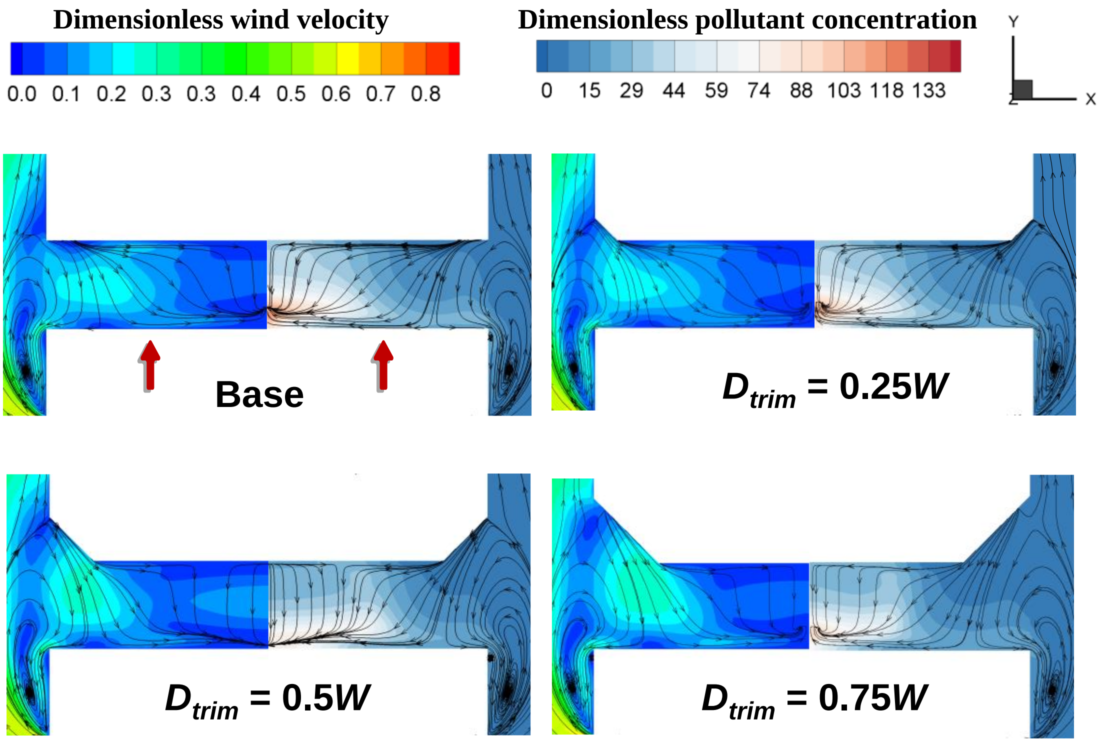

Fig. A4 Cross-comparison of the dimensionless wind velocity and pollutant concentration at the pedestrian level of a low-rise street canyon (H/W= 1 and L/W= 5) between the base case and design I case with different trimmed corner D_{trim}

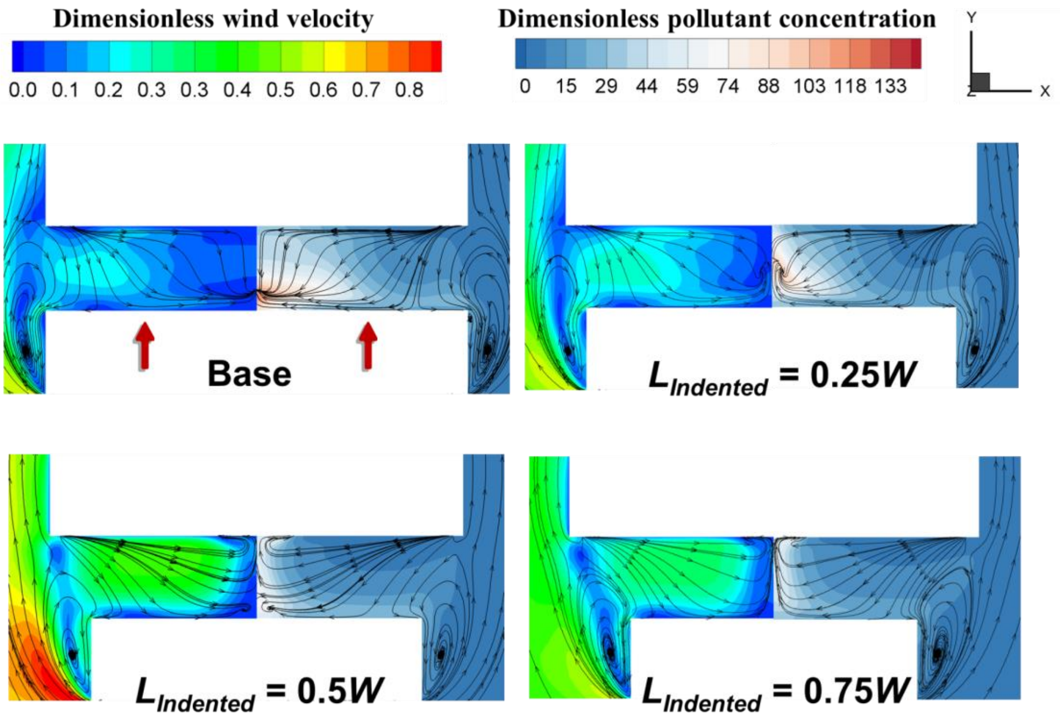

Fig. A5 Cross-comparison of the dimensionless wind velocity and pollutant concentration at the pedestrian level of a low-rise street canyon (H/W= 1 and L/W= 5) between the base case and design II case with different indented length $L_{indented}$

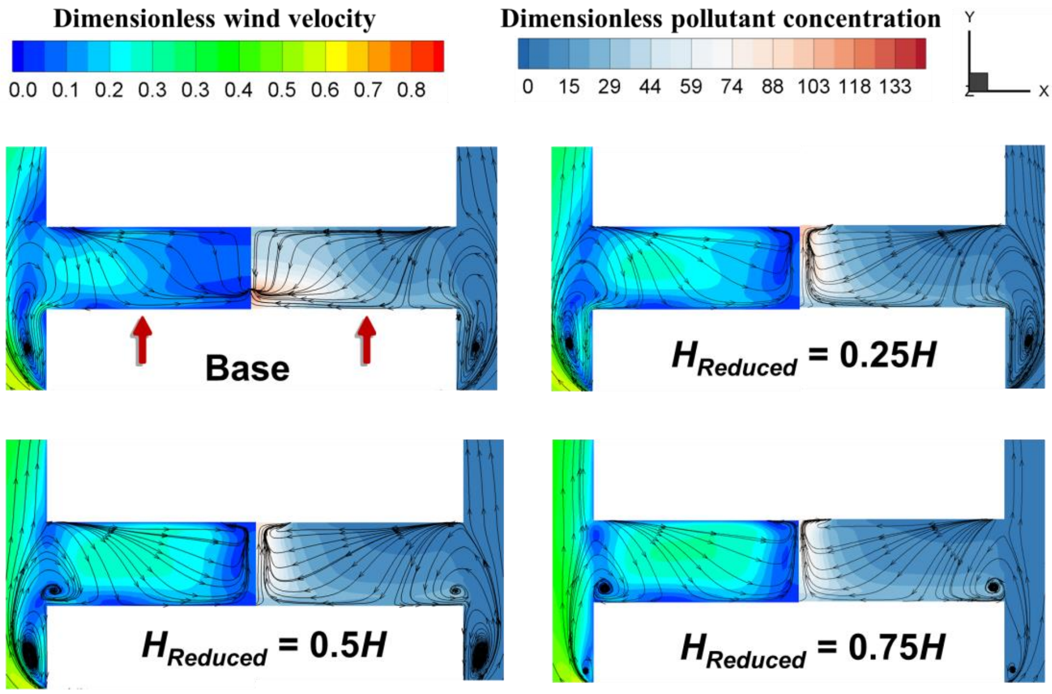

Fig. A6 Cross-comparison of the dimensionless wind velocity and pollutant concentration at the pedestrian level of a low-rise street canyon (H/W= 1 and L/W= 5) between the base case and design III case with different reduced height $H_{reduced}$

Table A1 Breathing rate for various age groups and microenvironments [51]

Breathing rate B_r (m^3/day)	Indoor at home (j= 1)	Other indoor location (j= 2)	Near vehicle (j= 3)	Other outdoor location (j= 4)
Children	12.5	14.0	14	18.7
Adults	13.8	15.5	15.5	20.5
Elderly	13.1	14.8	14.8	19.5